Dear Dr. Xinping Hu,

We appreciate the time and efforts you have dedicated on this review. We have accepted all the comments and made the proper changes in the manuscript (you can find them from the next page onwards) for final consideration to the Journal of Ocean Science.

We look forward to hearing back from you.

Sincerely,

Marta Veny

Biophysical coupling of seasonal chlorophyll-a bloom variations and phytoplankton assemblages across the Peninsula Front in the Bransfield Strait

Marta Veny [a], Borja Aguiar-González [a], Ángeles Marrero-Díaz [a], Tania Pereira-Vázquez [a], Ángel Rodríguez-Santana [a]

[a] Oceanografía Física y Geofísica Aplicada (OFYGA), ECOAQUA, Universidad de Las Palmas de Gran Canaria, Canary Islands, 35017, Spain

Correspondence to: Borja Aguiar-González (borja.aguiar@ulpgc.es)

Abstract. This study investigates the spatio-temporal variations of the chlorophyll-a (chl-a) blooms in the Bransfield Strait (BS) at a climatological scale (1998-2018). We propose that a suitable monitoring of these blooms can be achieved through remotely-sensed observations only if the BS is divided following the Peninsula Front (PF), which ultimately influences the phytoplankton assemblage. Our analysis is based on characterising climatological fields of Sea Surface Temperature (SST), air temperature, sea ice coverage, chl-a concentrations and wind stress, guided by synoptic novel and historical *in situ* observations which reveal two niches for phytoplankton assemblage: the Transitional Bellingshausen Water (TBW) and Transitional Weddell Water (TWW) pools. The TBW pool features stratified, less saline, warmer waters with shallow mixed layers, while the TWW pool features well-mixed, saltier, and colder waters. We identify that the 0.6ºC isotherm corresponds to the summertime climatological PF location, effectively dividing the BS in two different scenarios. Furthermore, the 0.5 mg m^{-3} chl-a isoline aligns well with the 0.6ºC isotherm, serving as a threshold for chl-a blooms of highest concentrations around the South Shetland Islands. These thresholds enable for the first time the monthly climatological descriptions of the two blooms developing in BS at both sides of the PF. We think this approach underscores the potential of combining SST and chl-a data to monitor the year-to-year interplay of the chl-a blooms occurring in the TBW and TWW pools contoured by the PF.

Keywords: Bransfield Strait, Chlorophyll-a bloom, Peninsula Front, Sea Surface Temperature, Biophysical coupling, Phytoplankton assemblage.

1 Introduction

Antarctic marine ecosystems are highly dependent on the seasonal cycle of the ocean-atmosphere interaction and associated sea ice dynamics (Schofield *et al*. 2010; Ducklow *et al*. 2013; Montes-Hugo *et al*. 2009; Sailley *et al*. 2013; Brown *et al*. 2019). Through this work we aim to characterise the seasonal variability of the biophysical coupling supporting the surface

30 chlorophyll-a bloom in the Bransfield Strait (BS), which is located in the Southern Ocean (SO) between the South Shetland Islands (SSI) and the Antarctic Peninsula (AP).

The BS is connected to the west with the Bellingshausen Sea and to the east with the Scotia and Weddell Seas (Figure 1). The confluence of water masses of different origin in this area leads to a highly dynamic system where different ocean
35 properties interact. Most of the previous studies have described the ocean surface dynamics of the BS based on summertime data (Figure 1a), when two inflows enter the strait and circulate cyclonically (Grelowski *et al.*, 1986; Hofmann *et al.*, 1996; Zhou *et al.*, 2006; Sangrà *et al.*, 2017). The horizontal and vertical structure of the summertime circulation and hydrography in the BS, when the chlorophyll-a bloom develops, may be summarised as follows.

40 The western inflow is the Bransfield Current (BC; Niller *et al.*, 1991; Zhou *et al.*, 2002, 2006) which is a coastal jet flowing to the northeast and transporting Transitional Zonal Water with Bellingshausen influence (TBW) along the southern slope of SSI. TBW is typically found within the first 300 m as a well-stratified and relatively warm (Θ > -0.4ºC) and fresh (<34.45) water (Sangrà *et al.*, 2017), seasonally originated in the Bellingshausen Sea and Gerlache Strait due to summer heating and ice melting (Tokarczyk, 1987; García *et al.*, 1994; Sangrà *et al.,* 2011). The eastern inflow is the Antarctic Coastal Current
45 (CC), which travels southwestward and transports Transitional Zonal Water with Weddell influence (TWW) in this area of Antarctica, countering the northern AP coastline. TWW is distinguished by colder (Θ < -0.4ºC) and saltier (>34.45) waters than TBW (Sangrà *et al.*, 2017), coming from the Weddell Sea (Tokarczyk, 1987; García *et al.*, 1994) and being rather homogeneous throughout the water column (Grelowski *et al.*, 1986; Hofmann *et al.*, 1996; García *et al.*, 2002; Zhou *et al.*, 2002). Between the BC and the CC, there is a street of mesoscale anticyclonic eddies (AEs) of TBW characteristics (Sangrà
50 *et al.*, 2011, 2017). Lastly, the BC recirculates around the islands, transporting TBW as a part of the summertime circulation (Sangrà *et al.*, 2017).

As will be analysed thoroughly in this work, at the encounter of TBW and TWW a key feature in the biophysical coupling of the chlorophyll-a bloom emerges, the Peninsula Front (PF; García *et al.*, 1994; López *et al.*, 1999). The PF is generally
55 formed at about 20-30 km from the AP slope as a mesoscale shallow structure of 10 km wide (Sangrà *et al.*, 2011) confronting TBW and TWW, and expanding from the surface down to ~100 m. On the opposite side of the BS, closer to the SSI slope, one finds the subsurface Bransfield Front (BF) between 50 to 400 m (Niller *et al.*, 1991; García *et al.*, 1994; López *et al.*, 1999), where TBW opposes TWW. The latter water mass widens its domain at depth over the whole strait. Generally, the BF extends between 10 to 30 km offshore from the SSI coastlines, being at its widest when approaching King
60 George Island (Veny *et al.*, 2022).

As for the bio-chemical context, SO waters are characterised by high-nutrient low-chlorophyll (HNLC) conditions which are equivalent to high concentrations of inorganic macronutrients, but low phytoplankton abundance and rates of primary

production (Mitchell and Holm-Hansen, 1991; Chisholm and Morel, 1991). Chlorophyll-a (chl-a) concentrations in the SO are frequently around 0.05-1.5 mg m^{-3} (Arrigo *et al*., 1998; El-Sayed, 2005; Marrari *et al*., 2006).

However, inshore waters west of the Antarctic Peninsula (wAP) are among the most productive regions of the SO (El-Sayed, 1967; Comiso *et al*., 1990; Sullivan *et al*., 1993). Thus, the chl-a concentration in the wAP differs from that found in the SO, with values ranging more extensively from 0.16 to 7.06 mg m^{-3} (Aracena *et al*., 2018). Yet, Hewes *et al*. (2009) reported that concentrations in this region are generally not higher than 3 mg m^{-3} based on satellite and *in situ* data. Previous studies, based mainly on summertime data (few during late-spring), have also characterised the spatial distribution of chl-a in the BS. The distribution was described as patchy and related to the spatial domain of each characteristic water mass (Basterretxea and Arístegui, 1999) and the Upper Mixed Layer (UML) depth, which reflects vertical stability (Lipski and Rakusa-Suszczewski, 1990; Hewes *et al*., 2009). Then, chl-a was found inversely correlated with UML depth and positively correlated with temperature, i. e. concentrations reach their maximums when UML depth is shallow, temperature is relatively high and surface waters are iron-replete (Hewes *et al*., 2009). More recently, García-Muñoz *et al*. (2013) reported that the highest phytoplankton concentrations along a cross-strait central transect in BS were correlated with relatively warm and stratified TBW waters. Nanophytoplankton (2–20 μm) was found to be predominant throughout the study area, which was dominated by small diatoms. However, haptophytes distribution co-varied with small diatoms and also appeared in well mixed TWW waters. As to diatoms, García-Muñoz *et al*. (2013) also identified a shift from smaller to larger diatoms when closer to the AP. Sharply, cryptophytes were restricted to stratified TBW waters. These authors concluded, for the first time in the literature, that phytoplankton assemblages around the SSI were strongly connected with the Bransfield Current System. This is the seed of our hypothesis: the horizontal extent of the surface signal of chl-a bloom in the BS may vary monthly from spring to summer (months of bloom development) according to the spatial distribution of the PF, through which TBW and TWW interact and embed different phytoplankton assemblages. This being confirmed, one could long-term monitoring the biophysical coupling between the surface chl-a bloom and the PF using remotely-sensed observations of chl-a and Sea Surface Temperature (SST).

Nevertheless, the chl-a distribution in high latitudes has also been reported to be coupled to other biophysical factors such as sea ice formation and atmospheric forcing. It is known that the seasonal sea-ice extent and its timing are likewise determinant for the chl-a development (Garibotti *et al*., 2003; Smith *et al*., 2008). Furthermore, sea ice conditions are influenced by atmospheric forcing such as the regional wind stress magnitude and direction, which vary from year-to-year (Smith *et al*., 2008). This manner, wind alterations significantly affect the sea-ice concentration around the West Antarctica (Holland and Kwok, 2012; Eayrs *et al*., 2019), although there are also seasonal and regional variations in the response (Kusahara *et al*., 2018).

Given the above scenario, one must confront that chl-a concentrations are not independently controlled by a single factor, and their temporal variations are complex, influenced by seasonal, intra- and interannual processes (Siegel *et al.*, 2002; Stenseth *et al.*, 2003); e. g. sea ice-ocean interactions may even evolve differently from one season to the next one (Stammerjohn *et al.*, 2012; Holland, 2014).

105
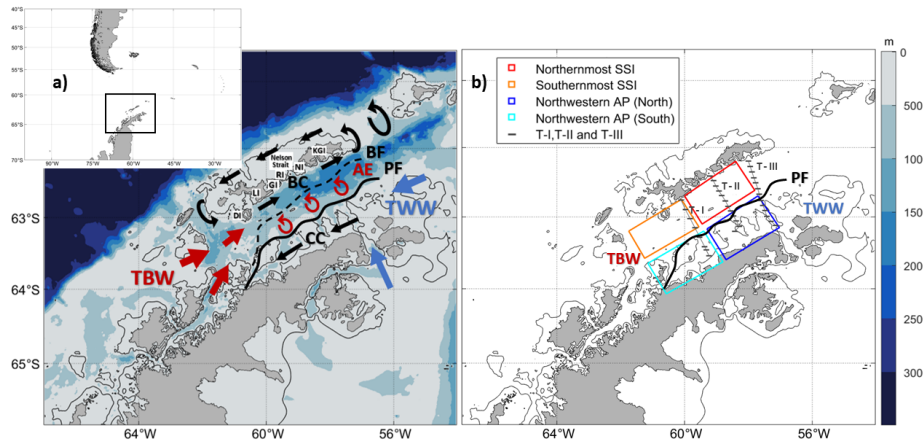
Figure 1. (a) Sketch of the circulation in the Bransfield Strait. Acronyms for South Shetland Islands (SSI) include DI (Deception Island), LI (Livingston Island), GI (Greenwich Island), RI (Robert Island), NI (Nelson Island) and KGI (King George Island). Acronyms for major oceanographic features are as follows: AE (Anticyclonic Eddy), BC (Bransfield Current), BF (Bransfield Front), CC (Antarctic Coastal Current), PF (Peninsula Front), TBW (Transitional Bellingshausen Water), TWW (Transitional Weddell Water); (b) Map showing cruise transects and boxes selected for dedicated analysis. The
110 transects are from two different oceanographic cruises and include T-I and T-III from CIEMAR (December 1999) and T-II from COUPLING (January 2010). Additionally, four boxes are defined between the SSI and the Antarctic Peninsula (AP): Northernmost SSI (red), Southernmost SSI (orange), Northwestern AP - North (dark blue) and Northwestern AP - South (light blue). The 200 m isobath is highlighted with a black contour in both panels.

115 In this work, we provide a comprehensive description of the seasonal variations of chl-a concentrations in the BS accounting for the biophysical coupling supporting its development. We hypothesize that this biophysical coupling is strongly conditioned by the spatio-temporal variability of the PF, as has been already argued.

The structure of this manuscript is as follows. In Section 2, we describe the data and methods. In Section 3, we present and
120 discuss the results distributed in four subsections. In Section 3.1, we set our hypothesis by analysing observational data from two oceanographic cruises: CIEMAR (December 1999) and COUPLING (January 2010). In Section 3.2, we construct

Deleted: working

satellite-based climatologies and examine the seasonally-varying horizontal distribution of SST, Sea Ice Coverage (SIC), chl-a concentrations, wind stress and Ekman pumping. In Section 3.3, we present the monthly evolution of the latter variables, along with air temperature, in order to characterise the spatio-temporal variability of the bloom according to four distinct regions (Figure 1b), which will be accounted for in the text. In Section 3.4, we address a review of works investigating the phytoplankton assemblage in the BS, bearing in mind the biophysical coupling previously described, in order to provide further insights based on the *state of the art* knowledge. Lastly, in Section 3.5, we construct satellite-based monthly climatologies of SST and chl-a along the same transects sampled during the CIEMAR and COUPLING cruises to present a climatological context to our hypothesis, through which the spatial distribution of the chl-a blooms in the BS varies according to the PF (monitored via SST), which contours the hydrographic area for TBW and TWW hosting different phytoplankton assemblages. Section 4 presents a summary of the main conclusions.

2 Data and methods

In situ observations and remotely-sensed measurements are detailed in the following, separately, for clarity. Seasons are defined following Zhang *et al.* (2011) and Dotto *et al.* (2021), as: summer (January-February-March), autumn (April-May-June), winter (July-August-September) and spring (October-November-December).

2.1 *In situ* observations: Antarctic cruises

The data inspiring the hypothesis that we address in this work, i. e. the spatial distribution of the chl-a bloom in the BS as strongly conditioned by the PF, rely to a great extent on Conductivity, Temperature, Depth (CTD) and fluorescence measurements collected from two interdisciplinary cruises: CIEMAR and COUPLING. The fluorescence measurements were collected with an ECO fluorometer, which measures fluorescence from chl-a, fDOM, uranine, rhodamine, and phycocyanin and phycoerythrin. In this work, we analyse the fluorescence from chl-a (Hernández-León *et al*., 2013; Sangrà *et al*., 2014).

On the one hand, the CIEMAR cruise was conducted in December 1999 (Corzo *et al*., 2005; Primo and Vázquez, 2007; Sangrà *et al*., 2011), and two transects covered the region from Livingston Island and King George Island towards the northern tip of the AP. On the other hand, the COUPLING cruise was conducted in January 2010 (Hernández-León *et al*., 2013; Sangrà *et al*., 2014; Sangrà *et al*., 2017), and a transect covered the region from Nelson Strait to the AP tip. Both cruises were carried out onboard the R/V BIO Hespérides. For further details about the CTD stations map of both cruises, the reader is referred to Sangrà *et al.* (2011) and Sangrà *et al.* (2017).

Additionally, *in situ* surface and subsurface (10 m depth) temperature measurements were downloaded from PANGAEA (https://www.pangaea.de/) and the World Ocean Database (WOD; https://www.ncei.noaa.gov/products/world-ocean-database) in order to assess the goodness of available open-access remotely-sensed products of SST and support the choice of the product providing the best fit. In Table A1 of the Appendix A, a summary of the cruises and corresponding dates for the CTD measurements used to this aim is presented.

2.2 Remotely-sensed products: Sea Surface Temperature and Sea Ice Coverage

We use satellite data of SST and SIC from the Operational Sea Surface Temperature and Ice Analysis (OSTIA; Good *et al*., 2020) downloaded from the Copernicus Marine Environment Monitoring Service (CMEMS; https://marine.copernicus.eu/) and developed by the United Kingdom Met Office. The motivation behind this choice is supported by a quantitative intercomparison between available SST open-access products and *in situ* temperature measurements (see this analysis in the Appendix A).

OSTIA provides the SST free of diurnal variability and the sea ice concentration. It is a reprocessed dataset with a high grid resolution of 0.05°, which accounts for both *in situ* and satellite data, and presents a processing level L4. This work analyses OSTIA data from 1998 to 2018.

2.3 Remotely-sensed products: Chlorophyll-a

We compute monthly climatologies of surface chl-a concentrations based on multi sensors/algorithms. The product name is OCEANCOLOUR_GLO_BGC_L4_MY_009_104, obtained from CMEMS (https://marine.copernicus.eu/). Chl-a data have a spatial and temporal resolution of 4 km and from 09/1997 to present, respectively, and a processing level L4. This work analyses concentrations from 1998 to 2018.

2.4 Remotely-sensed products: Wind and Air Temperature

We use the monthly averaged reanalysis of air temperature at 2 m and wind components at 10 m from ERA5 (Hersbach *et al*., 2020), which have a horizontal resolution of 0.25º over the period 1940 to present. From the wind components, we calculate the wind-stress and Ekman pumping.

We calculate the wind stress (τ), and wind stress zonal (τ_x) and meridional (τ_y) components, following Equations 1-3 (Patel, 2023):

$$\tau = \rho \cdot U_{10}^2 \cdot C_D ,\tag{1}$$

$$\tau_x = \rho \cdot U_{10} \cdot u \cdot C_D ,\tag{2}$$

185 $\tau_y = \rho \cdot U_{10} \cdot v \cdot C_D$, (3)

where ρ is the air density (1.2 kg m^{-3}); $U_{10} = \sqrt{u^2 + v^2}$ is the absolute value of the wind speed at 10 m above the surface (u and v are the eastward and northward wind speed components, respectively); x and y are the eastward and northward spatial coordinates; and, C_D is the drag coefficient, which is a function of wind speed, U_{10}. The equations used for wind stress computation are based on Gill (1982) formula and a non-linear C_D based on Large and Pond (1981), modified for low wind

190 speeds (Trenberth et al., 1990). We note that the mean C_D we obtained for our climatological maps in the BS is $1.4 \times 10^{-3} \pm 0.16 \times 10^{-3}$, analogous to the values reported by Kara et al. (2007) over the SO.

We also compute the Ekman vertical velocity as following:

$w_E = \frac{1}{\rho_0} curl\left(\frac{\tau}{f}\right)$, (4)

195 where ρ_0 is the water density (1025 kg m^{-3}); $f = 2\Omega sin\varphi$ is the Coriolis frequency (Ω is the Earth rotation rate, 7.2921×10^{-5} rad s^{-1}, and φ is the latitude). Positive (negative) w_E values indicate upward (downward) velocities leading to upwelling (downwelling).

3 Results and Discussion

Through this section we assess the major physical drivers potentially conditioning the vertical and horizontal structure of the

200 chl-a bloom in the BS. To this aim, in Section 3.1 we analyse the vertical and horizontal structure of two chl-a blooms in the BS based on hydrographic measurements from two cruises (1999 and 2010) along three cross-strait transects (T-I, T-II, T-III). In Section 3.2 we analyse the seasonal variations of the horizontal structure of the chl-a bloom and the PF from a climatological perspective based on remotely-sensed observations over a 21-year period (1998-2018): SST, SIC, wind stress and Ekman pumping. Next, in Section 3.3, we examine in detail the monthly climatologies of selected boxes of study in the

205 BS (adding air temperature to the analysis). In Section 3.4, we provide a summary review of the research on the phytoplankton assemblage in the BS. Lastly, in Section 3.5 we construct satellite-based monthly climatologies of SST and chl-a along the same locations as the transects T-I, T-II and T-III to provide a statistically robust (i. e. climatological) context to our hypothesis, through which the chl-a bloom extent varies according to the PF.

3.1 Vertical and horizontal structure along CIEMAR and COUPLING transects

210 We present the vertical structure of temperature, salinity, density, and fluorescence in the BS (Figures 2, 3 and 4) based on data collected during the multidisciplinary CIEMAR and COUPLING cruises through late-spring 1999 and early-summertime 2010, respectively. The physical oceanographic aspects from these cruises were firstly presented in Sangrà et al. (2011) and Sangrà et al. (2017).

Previous studies based on these measurements are in line with biophysical phenomena focused, among other aspects, on turbulence as a driver for phytoplankton distribution as well as on mesoscale physical features as key players in determining phytoplankton assemblages (García-Muñoz *et al.*, 2013; Macías *et al.*, 2013; Sangrà *et al.*, 2014). Following COUPLING cruise measurements, García-Muñoz *et al.* (2013) concluded that phytoplankton assemblages around the SSI were strongly connected with the Bransfield Current System. Furthermore, it was suggested that, considering the recurrence of the Bransfield Current System during the austral summer, the observed distribution of phytoplankton, which responded to this current system, should also be a quasi-permanent feature (García-Muñoz *et al.*, 2013). In the following, we combine the measurements from the two cruises for the first time to address this hypothesis, where we add and highlight that the key player appears to be the cross-strait gradient marked at surface by the PF, and that this may enable the long-term monitoring of the biophysical coupling between the surface chl-a bloom and the PF based on satellite measurements.

For clarity, we name the three transects of study as T-I, T-II and T-III moving from west to east. Thus, transect T-I (Figure 2) and T-III (Figure 4) correspond to CIEMAR and present novel measurements of fluorescence (not previously published); while transect T-II (Figure 3), located in between T-I and T-III, corresponds to COUPLING. The three transects originate over the shelf of the SSI and extend towards the AP running nearly perpendicular to the main axis of the strait. Notably, measurements from both sea trials agree well in showing a coherent vertical and horizontal structure of hydrography and fluorescence. In Figures 2-4, two panels are always dedicated to show the TS diagram and the station map to help the reader in following the ocean property descriptions.

Starting with T-I (Figure 2), this originates to the south of the Livingston Island and extends towards the AP. Along T-I, temperatures are above 0ºC in the upper 40 m for its full extent (Figure 2a), being relatively higher in the proximity of the SSI at a distance of 0-20 km and close to the AP, where they reach near surface values exceeding 0.6ºC and 0.4ºC, respectively. On the other hand, salinity is remarkably fresher and lighter near the SSI ($S < 34$ and $\sigma_\theta < 27.3$ kg m^{-3}), as opposed to saltier and denser waters towards the AP ($S > 34.3$ and $\sigma_\theta \sim 27.6$ kg m^{-3}; Figures 2b and 2c, respectively). Fluorescence levels exceeding 2-3 (Figure 2d) peak in the warmest (>0.2ºC) and lightest surface waters (upper 50 m) near the SSI (stations B1-B2) and near the AP (stations B5-B7). The isopycnal of 27.64 kg m^{-3} is highlighted in black in all vertical sections as a reference to the water mass boundary between TBW ($\sigma_\theta < 27.64$ kg m^{-3}) and TWW ($\sigma_\theta > 27.64$ kg m^{-3}; Sangrà *et al.*, 2011, 2017). These observations indicate the presence of relatively warmer TBW flowing near the surface to the south of Livingston Island. Coastal signals of Bransfield Strait Shelf Water (BS Shelf Water), characterised by lower salinity values (Zhou *et al.*, 2006; Polukhin *et al.*, 2021), were also detected. In addition, relatively colder TWW flows closer to the AP at deeper levels (> 60 m depth), where fluorescence sharply diminishes (< 0.5) along the entire transect (Figure 2d). The PF is not visible along T-I given the basin-wide extent of TBW at surface, which prevents shoaling of TWW.

¶
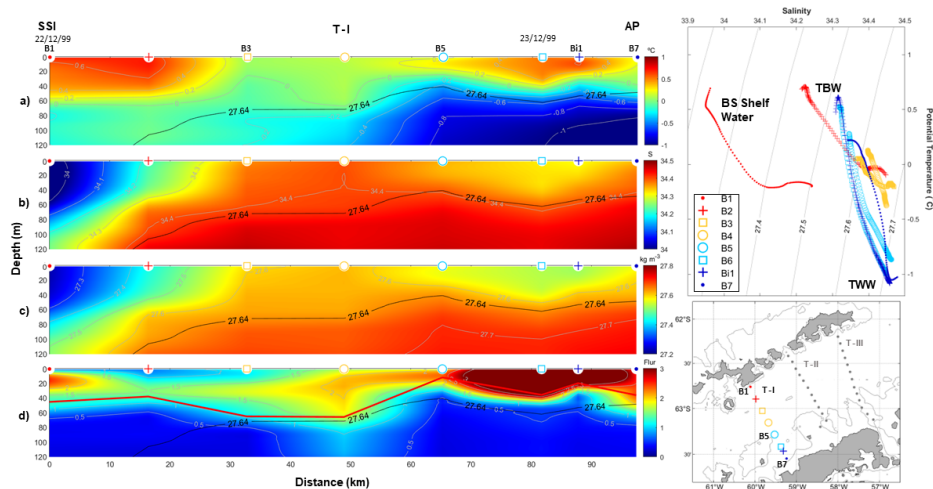
Figure 2. Vertical sections of ocean properties along transect T-I surveyed during the CIEMAR cruise (December 1999), running from Livingston Island to the Antarctic Peninsula. (a) Potential temperature, (b) salinity, (c) potential density, and (d) fluorescence are shown in the left-hand side panels. The solid black line represents the isopycnal of 27.64 kg m^{-3}, used as a reference to distinguish between Transitional Zonal Water with Bellingshausen influence (TBW) and Transitional Zonal Water with Weddell influence (TWW; Sangrà *et al*., 2017). The solid red line in panel d) shows the upper mixed layer depth computed following Holte and Talley (2009). The top right-hand side panel displays a Temperature-Salinity diagram to highlight water masses: Bransfield Strait (BS) Shelf Water, TBW, and TWW. Different marks and colours are displayed to represent data in each station. The bottom right-hand side panel shows a map depicting the stations of the transect T-I.

T-II (Figure 3) originates to the south of the Nelson Strait and extends towards the AP. Largely, along T-II, TBW waters are visible as warmer (Θ > -0.4ºC) and fresher (<34.45) than TWW (Sangrà *et al*., 2017). The subsurface signal of TWW extends towards the SSI, confronting TBW between 60-120 m depth at around stations 2-3, where they form the BF (Sangrà *et al*., 2011). Newly, the high fluorescence patch (> 1) extends within the warmest and freshest surface layers (Figure 3d) from the surface down to 60 m depth at its deepest, contouring the isotherm of 0.2ºC from the SSI until stations 9-10. At this location, the 0.2ºC isotherm reaches the surface, temperature decreases rapidly towards the AP (<-0.6ºC; Figure 3a), and salinity and density increase (>34.3 and >27.64 kg m^{-3}; Figures 3b and 3c). This gradient forms the PF, where TBW and TWW confront each other close to the AP. Remarkably, near surface (0-30 m) fluorescence levels decrease below 0.5 (Figure 3d) on the TWW side of the PF.
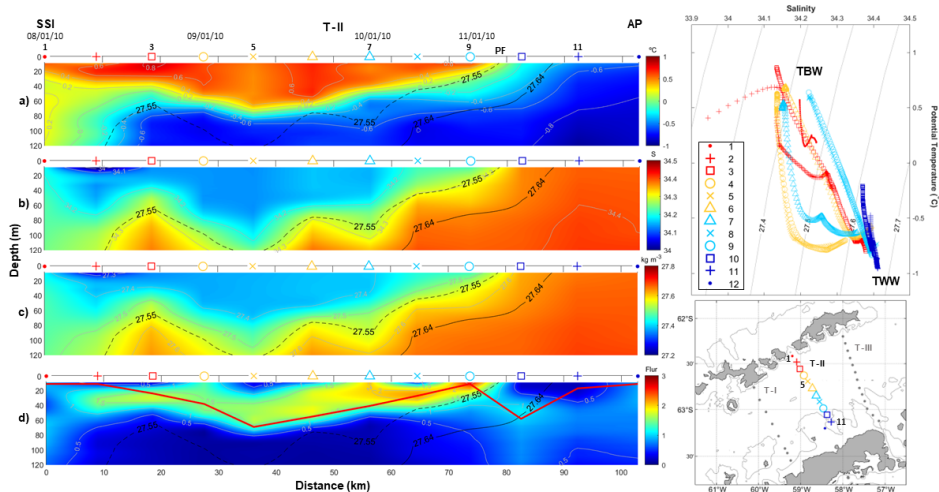
Figure 3. Same as in Figure 2 but for T-II, surveyed during the COUPLING cruise (January 2010) and running from Nelson Strait to the Antarctic Peninsula. Additionally, the dashed black line represents the isopycnal of 27.55 kg m^-3 which is used as a reference more adjusted to our dataset to distinguish between TBW and TWW.

Lastly, T-III (Figure 4) originates to the south of King George Island and extends towards the AP. Generally, we observe an analogous vertical structure to that described for T-II, suggesting that a horizontal coherence exists between transects; especially when accounting that differences with T-I are due to the latter is at a farther distance from the Weddell Sea and, hence, presents a weaker signal of TWW at surface. As observed in Figures 2 and 3, the chl-a bloom suggested by high fluorescence values (> 1) is again embedded within the pool of TBW closer to the SSI, where waters are relatively warmer and fresher as compared to TWW close to the AP. Newly, the PF (stations T10-T11) appears to delimit the surface easternmost reach of the patch with highest fluorescence. However, we must also note that, between the PF and the AP, a less prominent and coherent patch of values higher than the baseline exists down to nearly 120 m depth, both in T-II and T-III (fluorescence > 0.5 and >1, respectively).

Remarkably, two other studies (Basterretxea and Arístegui, 1999; Gonçalves-Araujo *et al*., 2015) have also captured a consistent cross-strait pattern where the highest chl-a concentrations are embedded within the TBW reservoir in the first ~60 m of the water column and the easternmost extent of this signal coincides with the location of the PF, through which TBW and TWW interact. In both cases, in spite of the sharp decrease of chl-a across the PF, chl-a concentrations were not low on

the TWW reservoir, but also relatively high although occupying a wider depth range (0-100 m). Their vertical sections were constructed from ship-based measurements collected along a transect parallel to T-III but farther north, departing from King George Island, in January 1993 and February-March 2009: Figure 6 in Basterretxea and Arístegui (1999); and, Figure 3 in Gonçalves-Araujo *et al.* (2015), respectively. This supports the existence of different phytoplankton assemblages occupying different niches according to the dominant water masses.
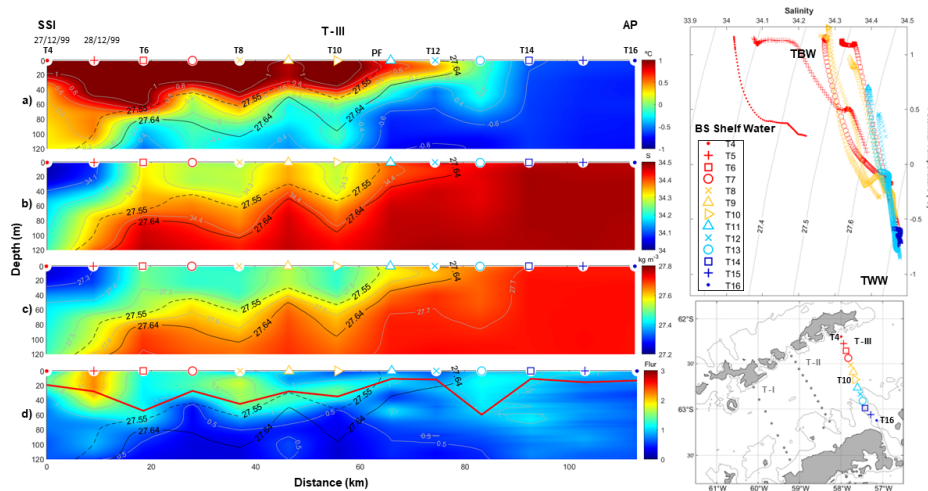
Figure 4. Same as in Figure 2 but for T-III, surveyed during the CIEMAR cruise (December 1999) and running from King George Island to the Antarctic Peninsula. Additionally, the dashed black line represents the isopycnal of 27.55 kg m^{-3} which is used as a reference more adjusted to our dataset to distinguish between TBW and TWW.

In all panels d) from Figures 2-4, a solid red line is added to indicate UML depth (Holte and Talley, 2009). Roughly, this estimate of the UML depth fits well with the depth of the high fluorescence patch embedded within the TBW reservoir, and which keeps phytoplankton under favourable light conditions, a better supply of dissolved iron (Prézelin *et al.*, 2000) and within a depth range with proper conditions for accumulation of phytoplankton biomass (Mukhanov *et al.*, 2021; Mendes *et al.*, 2023). Accordingly, relatively high fluorescence (>0.5) is accumulated along the entire BS in T-I, where UML depth is relatively shallow (<60 m), especially in stations B5-B7 (fluorescence above 2 and UML depths of ~15 m). The same pattern applies along T-II and T-III, with the high fluorescence patch embedded within the UML. In T-II, highest fluorescence (~2) is located near the PF, in station 9, where lowest UML depths occur (10 m). Similarly, in T-III fluorescence of 2 is closer to the SSI station 2 where UML depths are around 25 m. Moreover, near the AP, relatively low UML depths (10 m) are also observed in station T14 jointly with fluorescence of 1.

330   Following results in García-Muñoz *et al*. (2013), the fluorescence observations presented here from the COUPLING cruise (T-II in Figure 3) can be attributed to different phytoplankton assemblages, as briefly introduced in Section 1, namely: cryptophytes in the upper 60 m of the TBW reservoir between the BF and the PF; and, nanophytoplankton along the full transect but at higher abundances for the largest fraction in the TWW reservoir, accounting for the weaker but deeper signal in fluorescence (from the surface down to 100 m). This suggests that the fluorescence signal measured by the ECO

335   fluorometer might be dominated by cryptophytes. Whether this is also the case for the CIEMAR transects (T-I and T-III in Figures 2 and 4) is a feature we cannot confirm in absence of a phytoplankton assemblage study for that cruise. However, the fluorescence distribution appears consistent a decade apart in showing highest and shallower values within the relatively warm and stratified TBW reservoir, and lower but deeper values within the cold and well-mixed TWW reservoir. The stronger signal in fluorescence during the CIEMAR could be then attributed to a higher abundance of cryptophytes within

340   the TBW reservoir, if we assume that the pattern observed by García-Muñoz *et al*. (2013) is recurrent over time. Recent studies also support this by confirming the preferred niches of cryptophytes in the BS are the relatively warmer, less saline and stratified waters of the TBW reservoir, where they also compete with diatoms (Mendes *et al.*, 2013; Gonçalves-Araujo *et al.*, 2015; Mukhanov *et al*., 2021; Costa *et al*., 2023; Mendes *et al.*, 2023).

345   Results from the *in situ* measurements collected during the CIEMAR and COUPLING cruises, occurring a decade apart, plus more recent evidence of phytoplankton assemblages following the ocean dynamics of the Bransfield Current System jointly support further the basis of our hypothesis: the biophysical coupling between the spatial distribution of the surface chl-a bloom and the PF in the BS may be long-term monitoring using remotely-sensed observations of chl-a and SST.

350   In the following section, we analyse a set of satellite-based climatologies with the aim to demonstrate that the horizontal variability of the PF (and hence the interaction between TBW and TWW) plays a major role in determining the spatial extent of the patch with highest surface chl-a bloom in the BS. We complete this analysis by considering the role of several physical drivers which also contribute to set the niche for phytoplankton assemblage through a biophysical coupling. We expect this joint climatological perspective of the seasonal variations of the chl-a bloom and the PF, unprecedented in the

355   literature, provides the basis for their long-term monitoring. Counting with a robust long-term phytoplankton monitoring approach will enable a better understanding of the biophysical coupling setting the baseline of the marine food web in the BS.

3.2 Seasonal variations of the chl-a bloom and Peninsula Front coupling

    The remotely-sensed climatologies of SST, SIC, wind stress, Ekman pumping and chl-a were computed for the period 1998

360   to 2018, and are presented in Figures 5-8, respectively.

Regarding the SST (Figure 5), the most outstanding feature governing the summer months in the BS is a strong cross-strait gradient, where high temperatures (>1ºC) spread around the SSI and lower temperatures (<0ºC) appear to enter into the basin from the Weddell Sea, turning around the AP and spreading southwestward along the peninsula shelf. This strong temperature gradient is the surface signal of the PF, where TBW confronts TWW. Previous studies, based on *in situ*

370   summertime data, have used different thresholds for the isotherm characterising the location of the PF at surface, where TBW and TWW interact: Sangrà *et al.* (2017) used the isotherm of -0.4ºC, while Catalán *et al.* (2008) used the isotherm of 1ºC. The choice of these isotherms is not trivial and one must identify the isotherm embedding the water body flowing from the Weddell Sea into the BS, thus separating TWW from TBW. Looking at Figure 5a, we note the climatological isotherm characterising the PF location at surface during the summer months corresponds to 0.6ºC isotherm. Through autumn and

375   spring, the PF is also visible although a different isotherm rises as characteristic of this thermal front, being -1.2ºC and -0.8ºC, respectively. Lastly, during the winter months the surface signal of the PF vanishes, as one could expect, due to the atmospheric forcing prevailing in the homogenisation of the upper ocean. Within the strait, surface temperatures are around -1.8ºC ± 0.2ºC.

380   It is worthwhile noting that in Figures 3 and 4 we used the 0.2ºC and 0.8ºC isotherms, respectively, reaching the surface to define the location of the PF, and in Figure 5 we used a different isotherm. This is not in contradiction. One must keep in mind that the 0.2ºC and 0.8ºC characteristic isotherms worked well through synoptic transects, which took place in late December and January, while in Figure 5a a summertime climatological field is examined after time-averaging 3 data months over a period of 21 years. This accounts for the seasonally-varying values provided above, and which differ from the

385   synoptic values.

To the best of our knowledge, this is the first time that a remotely-sensed SST seasonal climatology is shown with the focus in the BS. In the Appendix A we present an examination of the goodness of SST satellite measurements against concomitant *in situ* measurements, finding that a high correlation exists between the product we use (OSTIA), and *in situ* measurements

390   ($R^2 = 0.849$). Also, the summertime field is in agreement with patterns reported in the literature for this season and based on *in situ* hydrographic measurements (Sangrà *et al.*, 2011, 2017). Additionally, we used a recently published seasonal climatology of hydrographic properties in the BS based on *in situ* measurements (Dotto *et al.*, 2021), and produced an analogous figure (not shown) to our Figure 5 (with the same contour lines and colorbar). The comparison supports the major features of the seasonal patterns described above. Exceptions occur north of the SSI in autumn and inside BS in spring,

395   where the abundance of mesoscale features in the climatology based on *in situ* measurements (Dotto *et al.*, 2021) slightly hampers the view of the mean field pattern.
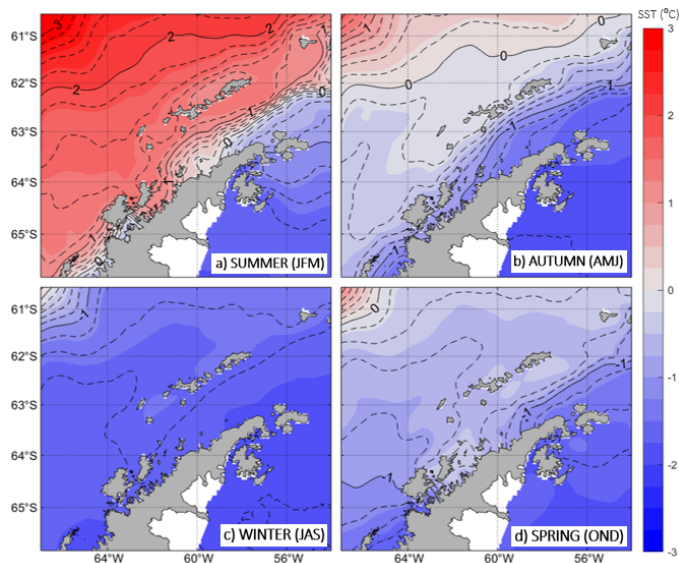
405

Figure 5. Seasonal maps of Sea Surface Temperature (SST; in shades of colours) for: a) summer, b) autumn, c) winter and d) spring. The capital letters between brackets stand for the initial letter of the month. The SST climatologies are averaged from January 1998 to December 2018. The dashed isotherms are plotted at intervals of 0.2ºC, while the solid line marks each 1ºC interval.

410   Figure 6 shows the seasonal SIC as a percentage of area covered by sea ice. A value of SIC about 15% is taken as indicative of the presence of sea ice. Thus, during the summer and spring months the BS is generally free of sea ice with SIC < 15%. Through autumn, the atmospheric forcing starts leading the development of the SIC in the BS, which extends firstly over the colder waters of the Weddell Sea intrusion with SIC ranging from 15 to 25% (compare Figure 5b and Figure 6b). This is in agreement with a recent study developed over the western AP, which addresses the role of subsurface ocean heat on the

415   modulation of the sea-ice seasonality, and highlights the importance of the upper ocean variability in setting sea-ice concentrations and thickness (Saenz *et al.*, 2023). Towards winter, the SIC is greater than 25% everywhere in the BS (Figure 6c), promoted by near-freezing sea surface temperatures around -1.8ºC ± 0.2ºC (Figure 5c).

Accounting that the seasonal sea-ice retreat is complete from spring to summer in the entire BS, this suggests that the larger

420   freshwater inputs reported in the literature over the TBW domain and contributing to the vertical stabilization of the water

Deleted: one can consider that

column, might be driven by a warmer oceanic forcing over coastal/glacial areas (Cook *et al.*, 2016) rather than by melting of the open ocean sea-ice.

425
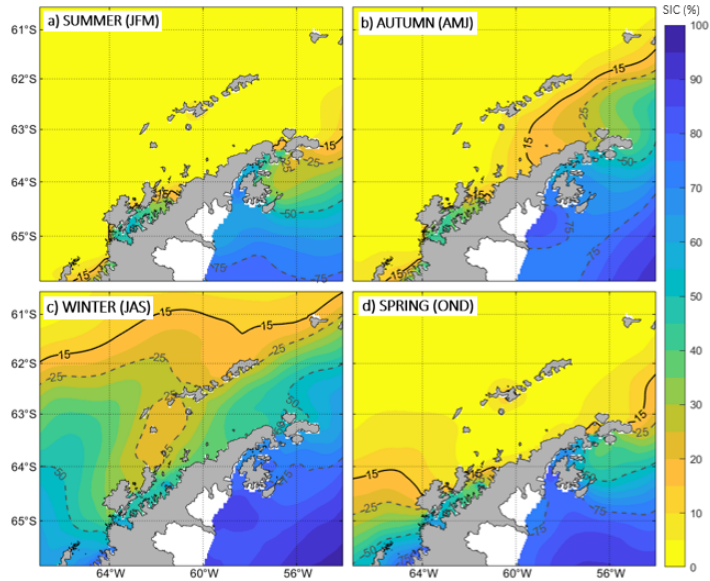
Figure 6. Same as Figure 5 but for Sea Ice Coverage (SIC). Solid black lines indicate a SIC percentage of 15%, which is the threshold to consider significant the presence of sea ice. Dashed grey lines represent SIC percentages of 25%, 50% and 75%.

430 Following seasonal panels in Figure 7, the development of the chl-a bloom in the BS is particularly revealing when using a logarithmic scale, which highlights spatial patterns otherwise slightly masked due to the strong signal of chl-a east of the AP in the Weddell Sea. West of the AP, chl-a bloom concentrations have been reported to range normally between 0.5-1 mg m^{-3} (Ducklow *et al.*, 2008; Smith *et al.*, 2008). However, we must note that this threshold varies significantly depending on the study region given that there are areas with naturally either higher or lower phytoplankton concentrations.

435

Generally speaking, the chl-a bloom in the BS starts developing in spring, reaching its maximum horizontal extent with values above 0.5 mg m^{-3} during the summer months, and still presenting patchy regions of high chl-a during autumn (Figure

7). We find that in the BS the isoline of 0.5 mg m^{-3} works well as the threshold contouring the chl-a bloom around the SSI, as this appears to embed coherently in space the region with highest chl-a values during the summer months. Through winter, surface chl-a concentrations drop below 0.25 mg m^{-3} everywhere in the BS except for the region adjacent to the northern shelf of the westernmost SSI (>0.25 mg m^{-3}). We observe that although the BS receives inflows from the Weddell Sea to the east of the AP, the much higher chl-a concentrations present in the Weddell Sea do not extend into the BS. This is in spite of the fact that the waters from the Weddell Sea are continuously propagating around the northern tip of the Peninsula and entering the BS. Notably, this feature persists year-round and the chl-a bloom never develops in the climatologies covering at its highest values the entire BS. Differently, at its largest extent, with values higher than 0.5 mg m^{-3} (summer months), the chl-a bloom appears constrained to the domain of TBW sourced from the Bellingshausen Sea while the presence of TWW marks the boundary where chl-a concentrations drop sharply within BS. By comparison between Figure 5a and Figure 7a, it becomes evident that the spatial extent of the surface chl-a bloom surrounding the SSI (chl-a > 0.5 mg m^{-3}) aligns well with the surface signal of the PF in the BS, where TBW and TWW confront each other. To ease visualization of this coupling, the isotherms of 1˚C and 0.6˚C have been added over the summertime chl-a field (Figure 7a).

This bloom area where chl-a concentrations are higher than 0.5 mg m^{-3} coincides in cross-strait direction with the chl-a bloom boundaries reported by García-Muñoz *et al*. (2013) for cryptophytes and large nanophytoplankton surrounding the SSI (their Figure 4). On the Drake Passage side, the oceanward extent of their bloom ended at the subsurface Shetland Front (García-Muñoz *et al*., 2013), embedding TBW over the northern shelf of the SSI, and accounting for the recirculation of TBW waters around the archipelago driven by the Bransfield Current (Sangrà *et al.*, 2017). In Figure 5a, the alignment of the subsurface Shetland Front to the north of the SSI is suggested by the isotherm of 1.6˚C, which roughly follows the oceanward extent of the surface chl-a bloom (Figure 7a). On the BS side, the chl-a bloom investigated in García-Muñoz *et al*. (2013) also transitioned towards lower values across the PF in agreement with this study (Figures 5a and 7a), and previous and later works (Basterretxea and Arístegui, 1999; Mendes *et al.*, 2013; Gonçalves-Araujo *et al.*, 2015; Mukhanov *et al.*, 2021). Lastly, we also note the resemblance of our summertime satellite-based climatologies of SST and chl-a (Figures 5 and 7) with those based on eighteen years of summertime hydrographic and chl-a measurements, through which Hewes *et al.* (2009) demonstrate that the distribution of high chl-a around the SSI corresponded to shallow UML depths in iron-rich waters at salinities ~34 (their Figure 4).

Deleted: waters

Deleted: waters

Deleted: the authors

Deleted: Hewes *et al.*, 2009;
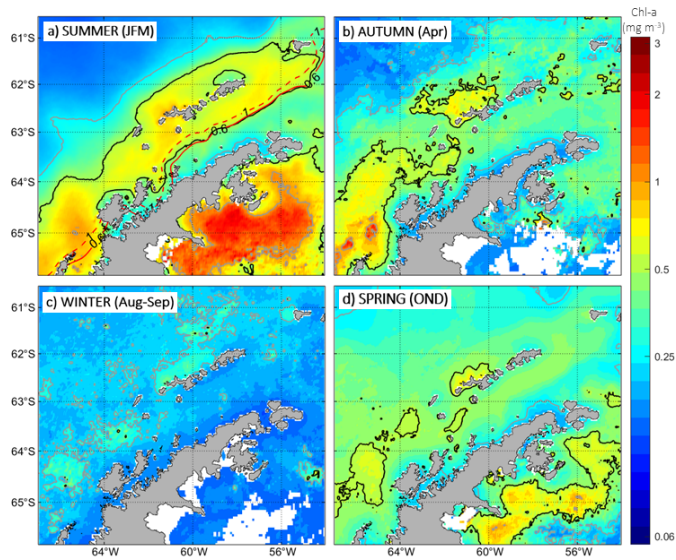
470

Figure 7. Same as Figure 5, but for chlorophyll-a concentrations (chl-a). Solid black lines indicate chl-a concentrations of 0.5 mg m^{-3}, while solid grey lines represent chl-a concentrations of 0.25 and 1 mg m^{-3}. Solid and dashed red lines in panel a) indicate 0.6ºC and 1ºC summer isotherms, respectively (see Figure 5a). For the autumn season (panel b), only the mean of April month is considered due to the absence of data during other months, which results from the presence of ice cover. Similarly, for the winter season (panel c), the mean of August and September months are solely considered for the same reason.

475
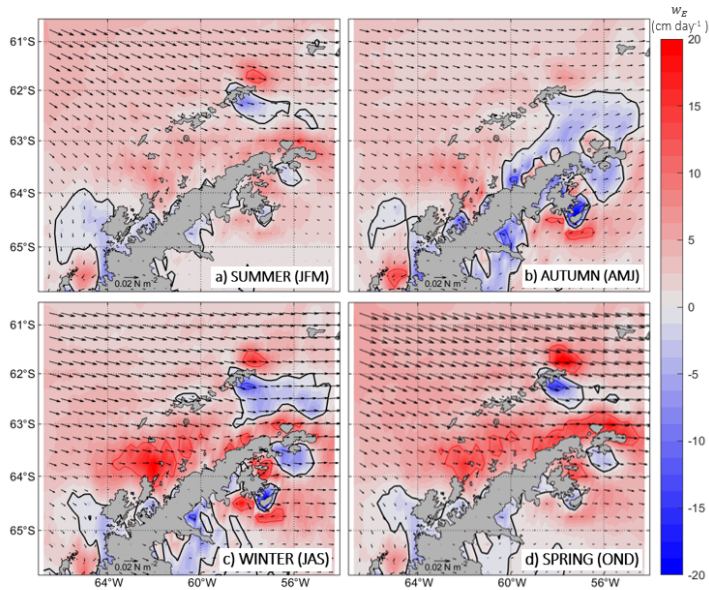
Figure 8. Same as Figure 5 but for Ekman pumping. Positive (negative) vertical velocities are indicated in shades of red (blue) and represent upwelling (downwelling) processes. Solid black lines refer to zero-velocities. Solid red and blue lines represent vertical velocities of 10 cm day^{-1} and -10 cm day^{-1}, respectively. Black vectors depict the wind stress. Wind stress reference vector is displayed over the southern AP with a value of 0.02 N m^{-2}.

480

In Figure 8, the seasonal climatology of the wind forcing acting over the bloom domain is presented following the wind stress field (black vectors) and Ekman pumping (vertical velocity; w_E). The dominant winds in the BS are the westerlies (Vorrath *et al.*, 2020), which flow across the strait with greater, basin-wide intensity during winter and spring months. In shades of colours, the Ekman pumping is shown with positive (red) and negative (blue) vertical velocity values implying that wind stress drives, respectively, either local upwelling or downwelling. Generally, upwelling is observed in the BS throughout the year, with a few spatial and temporal exceptions. Downwelling occurs mostly south of King George Island year-round. During autumn, this downwelling area south of King George Island expands towards the AP more extensively. This feature remains through the winter months although constrained to a smaller extent not reaching the AP. During winter and spring, the westerlies drive in the BS relatively strong upwelling vertical velocities especially along the shelf west of the AP.

490

Importantly, during spring and summer (months of chl-a development; Figures 7a and 7d), the westerlies appear slightly stronger along the southern shelf of the SSI (over the domain of TBW) as compared to westerlies acting over the shelf west of the AP (over the domain of TWW). Following this, one could reasonably expect deeper mixed layers over the domain where the wind stress forcing is stronger; however, along the southern shelf of the SSI winds favour the Bransfield Current transport of TBW via downwelling-favourable Ekman transport while, along the shelf west of the AP, winds exert a moderate counterforcing to the entrance of the Antarctic Coastal Current driving upwelling-favourable Ekman transport. We find this asymmetry may be contributing to maintain the two distinct niches across the PF: warmer, less saline and stratified waters transported by the Bransfield Current on the TBW side; and colder, saltier and well-mixed waters transported by the Antarctic Coastal Current on the TWW side.

3.3 Monthly variations of the chl-a bloom and Peninsula Front coupling

Following results from previous subsections, we note two areas in the BS are distinctive not only regarding their ocean dynamics as previously known (Figure 1), but also regarding the nature of the chl-a bloom. The first one is where the chl-a bloom spreads with highest concentrations over the relatively warmer and more stratified TBW water, flowing northeastward along the southern shelf of the SSI. The second one is the relatively colder and more homogeneous TWW waters flowing southwestward along the western shelf of the AP.

For further study of the monthly evolution of ocean and atmospheric conditions influencing the development of the surface chl-a bloom over each area, we divided the BS into four boxes of study (Figure 1b). These boxes were designed to capture, respectively, the northern and southern domain of the surface chl-a bloom embedded in TBW south of the SSI, and northern and southern domain of the surface chl-a bloom embedded in TWW west of the AP. The resulting climatologies of SST, air temperature, SIC, chl-a, along-shore wind stress and Ekman pumping over the period 1998-2018 are presented in Figure 9 and reveal several spatio-temporal similarities, and differences, which stand out and provide further insights. To this aim the wind stress was decomposed into its along-shore ($\tau_{x'}$) and cross-shore ($\tau_{y'}$) components through rotation of the cartesian components 36.25º in counterclockwise sense.

The monthly climatologies of SST and air temperature (Figures 9a and 9b) present a coherent seasonal cycle where warmer (colder) temperatures are found within all the regions for summer (winter) months. Spatially, SST within the boxes south of the SSI are generally warmer than those along the west AP. This is more prominent during summer months, when cross-strait temperature gradients are higher with differences between boxes at opposites of the strait about 0.6ºC to 1.4ºC (Figure 9a). These differences decrease towards the winter months, when all regions approach at surface near-freezing temperatures about -1.8ºC from July to August. Evolving through the spring months, temperature differences start to increase again but are

not higher than 1ºC when comparing boxes along the southern shelf of the SSI and along the shelf of the AP. Because boxes south of the SSI, sourced by TBW, depart from higher temperatures and all regions reach near-freezing temperatures during winter, their seasonal amplitudes are larger (and the slopes are more pronounced) as compared to boxes along the shelf of the west AP, sourced by TWW. Thus, the seasonal amplitude of the SST is more than 1.5 times larger for the southern shelf of the SSI (~3ºC) than along the west AP shelf (~1.8ºC).

The seasonal amplitude of the air temperature cycle (Figure 9b) is larger than that displayed in SST. However, warmer temperatures are once again observed in the boxes situated along the southern shelf of the SSI, where temperatures evolve from 1ºC (summer) towards -5º to -6ºC (winter), in contrast to the boxes situated along the west AP shelf, where temperatures evolve from 0ºC (summer) towards -8ºC (winter). As compared to the SST annual cycle, we observe the air temperature is more homogeneous during the summer and spring months (temperature differences among boxes are < 1.25ºC) than during autumn and winter (temperature differences among boxes are > 2.5ºC). This is the reverse pattern as shown in SST, where more homogenous temperatures among regions were found through the winter months. The reason behind the more homogeneous pattern in SST during the winter months may be due to sea water approaching near-freezing temperatures, what sets a threshold which homogenizes the ocean surface under an extreme cooling atmospheric forcing.

The SIC monthly climatology (Figure 9c) follows an inverse relationship with SST and air temperature (Figures 9a and 9b), where higher values of SIC are found during late autumn, winter and early spring months and absence of sea ice is found through late spring, summer and early autumn months (<15% SIC). Through these latter seasons, the sea ice retreat is driving melting waters into the environment. This is a key factor in phytoplankton biomass accumulation since it allows upper ocean stratification during spring/summer, leading to favourable sunlight conditions for phytoplankton to grow (Ducklow *et al*., 2013). Then, the SIC peaks in July at about 50% closest to the AP tip, at about 40% farther south along the AP and south of the northernmost SSI. One month later the SIC peaks in August at about 30% south of the southernmost SSI.

Remotely-sensed chl-a observations enable the visualization of the monthly evolution from August to April (Figure 9d) with a data gap due to sea ice coverage from May to July. Yet, a seasonal cycle is visible with higher chl-a concentrations through spring and summer months; lower, and declining, chl-a concentrations through early autumn; and, lower, and increasing, chl-a concentrations through late winter. This latter increasing trend is concomitant to the decrease in SIC, when sea ice starts melting in August (same month when SST and air temperature also start increasing). Following the literature, the date of the bloom initiation is determined as the first day at which chlorophyll levels rise a 5% above the climatological median (Siegel *et al*., 2002) and stays above this value for at least two consecutive weeks (Thomalla *et al*., 2011). This threshold was computed assuming linear interpolation over winter to get the climatological median. Bearing these criteria in mind, our climatologies indicate the chl-a bloom in the BS starts through mid-October, departing from a baseline for chl-a concentrations ~0.2 mg m^{-3} in August. Since mid-October (early spring) onwards, chl-a concentrations start increasing in the

entire BS although more steeply along the southern shelf of the SSI, and slightly delayed in the northern box of the western shelf of the AP.

Chl-a peaks through December and February at 0.68 mg m^{-3} south of the southernmost SSI and in February at 0.63 mg m^{-3}
565   south of the northernmost SSI (Figure 9d). Along the shelf of the west AP, chl-a peaks to the south in December at 0.43 mg m^{-3}; and, one month later, to the north in January at 0.37 mg m^{-3}. Generally, although standard deviations are large and overlap each other cycles, these monthly climatologies suggest a northward development for the chl-a peaks with about 1-2 months of delay.

570   The pattern described above for the four boxes of study supports the likely existence of two different chl-a blooms developing simultaneously but of different *nature* (i. e. phytoplankton assemblage) in the BS, as suggested by their different intensity and timing (month of initiation and rate of increase). This is in agreement with former results in a series of studies which reported that cryptophytes compete in the BS primarily with diatoms and other nanophytoplankton groups (Mura *et al.*, 1995; García *et al.*, 2013; Mendes *et al.*, 2013; Gonçalves-Araujo *et al.*, 2015; Mukhanov *et al.*, 2021; Costa *et al.*, 2023;
575   Mendes *et al.*, 2023), following strategies to adapt better to water mass distribution in the basin, what ultimately controls the time and space variability of BS phytoplankton communities.

Only two former studies have reported monthly climatologies of the surface chl-a bloom in the BS; however, none of them framed the boxes of study such that the two blooms were simultaneously, and distinctively, captured. In the first study,
580 Gonçalves-Araujo *et al.* (2015) placed a rectangular box embedding at the same time both margins of the BS, with no distinction between the TBW and TWW domains. The resulting time-series (2002-2010) displays a strong interannual variability, with summertime values ranging from ~ 1.1 mg m^{-3} (2006) to 0.37 mg m^{-3} (2003; their Figure 9). In the second study, La *et al.* (2019) placed a slanted rectangular box parallel to the SSI coastline, and similar to our two boxes south of the SSI, but in their case extended towards Elephant Island. The resulting monthly climatology of the chl-a over the period
585   2002-2014 (12-year mean) displays the cycle from October to April. The chl-a bloom develops then from baseline concentrations below 0.2 mg m^{-3} in October to peak concentrations ranging from ~ 1.75-1.95 mg m^{-3} (their Figure 2) through February to March. We attribute the higher climatological values in La *et al.* (2019), occurring about one month later than in our boxes along the SSI, to the different choice of the study area. In their case the northward extension of the box may be including dynamics out of the BS, from the confluence zone with the Weddell Sea. Also, the latter peak in time for this
590   extended region is in agreement with our results in Figure 9d, which suggests the maxima in chl-a develops later as one moves northward along the BS.

Finally, the along-shore wind stress (Figure 9e) displays year-round downwelling-favourable winds along the southern shelf of the SSI and upwelling-favourable winds along the shelf of the west AP. In all cases, a quarterly cycle stands out with

---

maxima values (in descending order) in September, December, February and May (i. e. winter, spring, summer and autumn).

600 A similar cycle is found along the shelf of the west AP for the Ekman pumping (Figure 9f), where vertical velocities are upwelling favourable (positive) year-round with a quarterly cycle (same maxima time variability). Along the southern shelf of the SSI, vertical velocities are also upwelling favourable (positive) year-round but less intense and more homogenous through seasons. Peak vertical velocities are 20 cm day^{-1}, 17.5 cm day^{-1} and 5 cm day^{-1} for boxes along the shelf of the west AP, south of the southernmost SSI and south of the northernmost SSI, respectively.

605
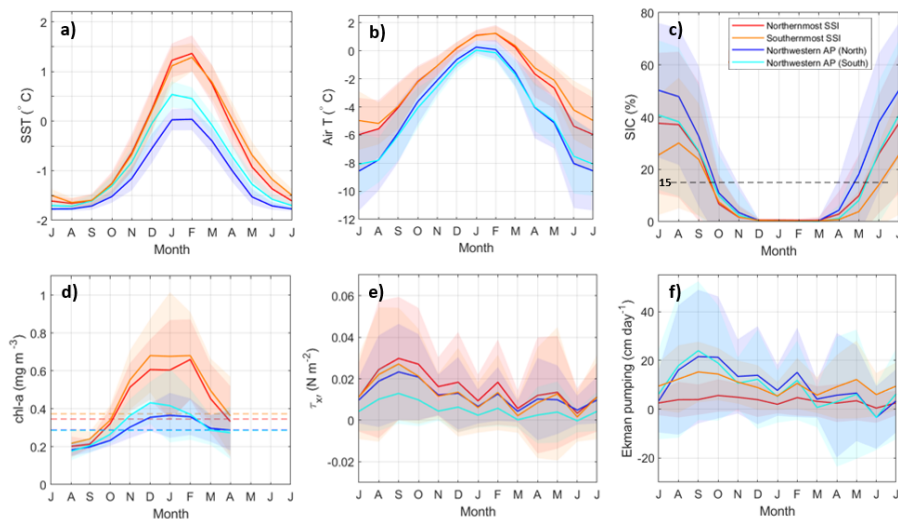
Figure 9. Monthly climatology over the period 1998 to 2018 of a) Sea Surface Temperature (SST), b) air temperature, c) Sea Ice Coverage (SIC), d) chlorophyll-a (chl-a) concentration, e) along-shore wind stress, and f) Ekman pumping (vertical velocity) for each study box, as delimited in Figure 1b. The horizontal dashed lines in panel c) indicate the threshold (15%) to consider significant the presence of sea ice, while in panel d) indicate the threshold set to

610 identify the initiation of the bloom following Siegel *et al.* (2002) and Thomalla *et al.* (2011). The mean monthly values are represented by the solid line, while the corresponding standard deviation is shown in coloured shades.

3.4 Spring-Summertime phytoplankton assemblages of the chl-a bloom: Historical observations

Through the previous section, we have learned that a proper design of study boxes aligned with the climatological

615 summertime position of the PF enables the identification of two distinct chl-a blooms in the BS based on satellite

measurements according to two water mass scenarios: TBW and TWW. In this section, we review more than three decades of previous studies and indicate their main findings in Table 1, so that we can discuss them thoroughly and identify common patterns observed in the past.

620

In summary, existing observations listed in Table 1 support that the phytoplankton community in the BS responds to a variety of factors which may vary from year to year, thus introducing high interannual variability in the phytoplankton assemblage. The factors primarily driving the nature of the chl-a bloom are: (1) vertical stability of the water column; (2) the depth of the UML, which influences the penetration of light into the depth range where biomass may accumulate near the surface; (3) the existence of sea-ice retreat, supplying relatively cold freshwater to the environment; and, (4) the grazing pressure of herbivorous zooplankton. Berdalet *et al.* (1997) already accounted for these four factors and reported that the combination of those appear to play a major role in the development, accumulation and spatial variability of microplankton biomass. After reviewing the most recent studies, we confirm this statement still holds in water and applies also to at least the nanophytoplankton size (there is a scarcity of works investigating the picophytoplankton along cross-strait transects in the BS so that we cannot extend here the statement robustly to this phytoplankton size). Interestingly, these physical factors may also condition the phytoplankton succession through a given bloom season and, thus, small cells appear to dominate the phytoplankton community structure during spring as large cells develop to form blooms in summer months (Petrou *et al.*, 2016).

635 In this context, it is worthwhile highlighting the results from two studies employing multi-year datasets of *in situ* observations of phytoplankton assemblage in the BS through four (Gonçalves-Araujo *et al.*, 2015) and nine (Mendes *et al.*, 2023) different bloom seasons, respectively.

On the one hand, in the first study, Gonçalves-Araujo *et al.* (2015) investigated microplankton (20-200 μm) and
640 nanoplankton (2-20 μm) through summertime of 2003, 2004, 2008 and 2009, identifying three main taxonomic groups within the study area: diatoms, flagellates and cryptophytes. From year to year, the surface distribution of phytoplankton size was dominated by nanoplankton in 2003, 2004 and 2008 (>80% of the total chl-a) with no clear cross-strait gradient. Differently, in 2009 the surface distribution of chl-a presented two distinct domains: (1) in the TBW pool, a mixed community of microplankton and nanoplankton at high (~50-70%) and low (~30-50%) percentages of the total chl-a,
645 respectively; and, (2) in the TWW pool, a reversed mixed community of nanoplankton and microplankton at high (~80%) and low (~20%) percentages of the total chl-a, respectively. Regarding the taxonomic groups, Gonçalves-Araujo *et al.* (2015) found that interannual variability in species composition resulted from an alternation between diatom-dominated and flagellate-dominated assemblages: 2003 and 2004 were dominated by cryptophytes nearly everywhere in the BS, 2008 by flagellates; and, 2009 by a mixture of diatoms close to the SSI and flagellates close to the AP.

650

Interestingly, in the second study, Mendes *et al*. (2023) investigate a subsequent period of time (2008-2018) based on measurements from nine different years (2011 and 2012 are absent) and demonstrated a strong coupling between biomass accumulation of cryptophytes, summer upper ocean stability, and the mixed layer. Through 2008-2018, Mendes *et al*. (2023) report that cryptophytes present a competitive advantage in environments with significant light level fluctuations, normally found in confined stratified upper layers, and supported that observational finding with laboratory experiments where cryptophytes revealed a high flexibility to grow in different light conditions driven by a fast photo-regulating response. These results provided the basis to understand why the environmental conditions promoted the success of cryptophytes in coastal regions, particularly in shallower mixed layers associated with lower diatom biomass, and highlighted a distinct competition or niche separation between diatoms and cryptophytes. Over the long-term variability, Mendes *et al*. (2023) concluded that cryptophytes are gradually outgrowing diatoms along with a decreased size spectrum of the phytoplankton community. This is in agreement with recent results supporting that the increasing melt-water input in the BS can potentially increase the spatial and temporal extent of cryptophytes (Mukhanov *et al.*, 2021), which benefit from the higher stabilization of the water column driven by the freshwater input.

This reported shift towards a higher abundance of cryptophytes over diatoms is not trivial and, if persists in time, it will eventually impact the biogeochemical cycling in Antarctic coastal waters due to a shift in trophic processes (Mukhanov *et al.*, 2021). The latter work poses the scenario as follows. The replacement of large diatoms with small cryptophytes favours consumers like salps over Antarctic krill. Salps, a food competitor of Antarctic krill, can feed a wide range of taxonomic and size compositions of phytoplankton prey. Thus, salps present a much lower feeding selectivity (Haberman *et al.*, 2003) than Antarctic krill, which presents positive selectivity for diatoms (large prey) and avoid cryptophytes (smaller prey) when feeding on complex prey mixture (Haberman *et al.*, 2003). The shift towards an increasing role of cryptophytes in BS waters would then lead to constraints in food supply for krill, strengthening the abundance of its competitor. This would not only threaten Antarctic krill populations, but also higher consumers including penguins, seals, and whales, which feed on krill (Loeb *et al.*, 1997).

Based on the above discussion, we find that the biophysical coupling between the chl-a blooms at both sides of the PF is largely the result of interannually varying physical properties determined by the TBW and TWW pools, and that some of those physical properties could be easily monitored via remotely-sensed observations such as: (1) SST to control the extent of the TBW and TWW pools; and, (2) SIC to monitor the sea-ice budget and sea-ice retreat as source of vertical stability to the water column. Through the last section of this study, we attempt to highlight that monitoring the spatio-temporal distribution of the chl-a blooms in the BS according to satellite measurements of SST and chl-a may represent a pivotal knowledge in future studies about the potential causes driving the long-term variability of the phytoplankton assemblage across the PF.

Reference	Methodology	PFTs in TBW	PFTs in TWW	PFTs in Bransfield Strait	Date
Mura *et al.*, 1995	Fluorometric method and microscopy analysis.	Highest relative contribution to community biomass by eukaryotic picoplankton and DTs.	Highest relative contribution to community biomass by eukaryotic picoplankton and DTs.	The highest abundance across the PF was attributed to CPs.	1993 (summer).
Berdalet *et al.*, 1997	Fluorometric and biochemical methods to determine microplankton biomass.	The highest values of MP biomass indicators (chl-a, ATP and protein) were found in ice-melting waters and TBW.	The lowest values of MP biomass indicators (chl-a, ATP and protein) were found in TWW.	The degree of stabilization of the water column, the depth of the UML and the grazing pressure of herbivorous zooplankton play a major role in the development, accumulation and spatial variability of MP biomass.	1994, January (summer)
García-Muñoz *et al.*, 2013	Flow cytometry, FlowCAM, HPLC/CHEMTAX pigment analysis.	Highest abundance of CPs and relatively high abundance of NP (large size).	Higher abundance of NP (large size) and lower abundance of NP (small size).	High abundance of NP (medium size) across the PF.	2010, January (summer)
Mendes *et al.*, 2013	HPLC, CHEMTAX, microscopy analysis.	--	--	Dominance of DTs in deeper UML, higher salinity and warmer SST.	2008-2009 (late summer).
	HPLC, CHEMTAX, microscopy analysis.	--	--	Dominance of CPs in shallower UML, less salinity and colder SST (cold summer with late ice retreat). Low diatom biomass in presence of high nutrient concentrations (particularly silicate) and low chl-a.	2010 (late summer).
Gonçalves-Araujo *et al.*, 2015	Either fluorometric or spectrofluorometric method, and microscopy	Dominance of microplanktonic DTs associated with higher	Dominance of nanoplanktonic flagellates (CPs, HPs)	Interannual variability of chl-a bloom is governed by alternation between	2003, 2004, 2008, 2009 (summer).

		chl-a in shallower UML.	associated with lower chl-a in deeper UML.	diatom-dominated and flagellate-dominated assemblages.	
Mukhanov *et al.*, 2021	Flow cytometry, fluorescence.	Presence of CPs (9μm) and other NP (<3μm). Highest CP abundance and biomass are found in the photic layer around the jet of the Bransfield Current.	CPs were scarce or undetectable.	--	2020, January (summer).
Costa *et al.*, 2023	HPLC, CHEMTAX, microscopy analysis.	--	--	Equivalent proportion and abundance of smaller nanoflagellates (CPs, DNs, *P. antarctica* and green flagellates), and centric and pennate DTs. CPs prefer low salinities, and centric DTs prefer higher salinities (>34). DNs and centric DTs prefer deeper UML.	2013-2014, 2014-2015, November (spring) .
	HPLC, CHEMTAX, microscopy analysis.	--	--	Low diatom biomass accumulation. Higher proportion of CPs, DNs and/or pennate DTs with background presence of mixed flagellates. CPs and pennate DTs prefer shallow UML, but CPs occupy colder waters than pennate DTs.	2013-2014, 2014-2015, (spring/summer).
	HPLC, CHEMTAX, microscopy analysis.	--	--	High diatom biomass accumulation dominated by centric DTs.	2015-2016, (spring/summer).
Mendes *et al.*, 2023	HPLC, CHEMTAX, SEM, DNA sequencing and phylogenetic inference.	--	--	CPs are gradually outgrowing DTs along with a decreased size spectrum of the phytoplankton community.	2008-2018 (summer).

Table 1. Historical observations investigating the chlorophyll-a bloom in the Bransfield Strait and reporting a description of the phytoplankton assemblage either by water mass domain (TBW or TWW) or without distinction. We must note that in none of the studies the full spectrum of Phytoplankton Functional Types (PFTs) is covered, and so this review attempts to provide a general overview of the existing knowledge. Acronyms for PFTs sizes are as follows: microphytoplankton (MP; 20-200 μm), nanophytoplankton (NP; 2-20 μm), picophytoplankton (PP; 0.2-2 μm). Other acronyms for PFTs are: diatoms (DTs), cryptophytes (CPs), haptophytes (HPs), dinoflagellates (DNs). Lastly, acronyms for methodology are: High Performance Liquid Chromatography (HPLC), Chemical taxonomy (CHEMTAX) software v1.95 (Mackey *et al.*, 1996), Scanning Electron Microscopy (SEM).

3.5 Monthly variations of SST and chl-a along the CIEMAR and COUPLING transects

As a closure to our analyses we return to the synoptic transects which motivated our hypothesis, based on *in situ* hydrographic and fluorescence measurements (T-I, T-II and T-III; Figures 2-4), and construct spatio-temporal climatologies of remotely-sensed SST and chl-a along the same transects (a series of black dots denote for reference the spatio-temporal position of the hydrographic stations along the Hovmöller diagrams in Figure 10). The aim is to highlight that the monthly variability of the easternmost extent of the chl-a bloom in the TBW pool and the westernmost extent of the chl-a bloom in the TWW pool responds closely to the monthly variability of the PF. We think this approach supports further the potential of long-term monitoring the observed biophysical coupling via remotely-sensed measurements when study boxes are properly placed according to governing ocean dynamics.

From early spring (October) to early autumn (April), the PF emerges prominently along transects T-II and T-III (Figure 10a), where relatively warm TBW, richer in chl-a along the southern shelf of the SSI (SST > 1.4ºC; chl-a ~ 0.7-0.8 mg m^{-3}) opposes relatively colder TWW and poorer in chl-a (SST ~ -0.2º to -0.6ºC; and chl-a < 0.3-0.4 mg m^{-3}) along the western shelf of the AP (Figure 10b).

It is worthwhile noting that the PF delineated along the synoptic transect T-II, found between stations 9-10 (Figure 3), corresponds closely to the climatological location of the PF (0.6ºC and 0.5 mg m^{-3}) observed between stations 8-9 (Figure 10a). Similarly, along T-III, both the hydrographic and the climatological PF are found at the same position, between stations T10 and T11.

As it occurred along the synoptic transect T-I (Figure 2), the PF is not visible along the climatological transect T-I (Figure 10a), where relatively warm TBW invades the strait, and the TWW signal is absent from early spring (October) to early autumn (April) with SST values ~ 0.2ºC. The absence of a strong cross-strait temperature gradient along T-I is in agreement with an elongated patch of high chl-a concentrations which expands towards the western shelf of the AP, reaching values ~ 0.5 mg m^{-3} as far east as 84 km offshore the SSI (Figure 10b). This is analogous to the basin-wide, high fluorescence signal shown along the synoptic transect T-I in Figure 2.

725   Throughout the remainder of the year, both SST and chl-a values follow similar patterns along the three climatological transects (T-I, T-II and T-III), displaying basin-wide, lower and more homogeneous values.

Notably, the highest chl-a concentrations are always found offshore along the three climatological transects, embedded in patches of warmest TBW (SST > 1.2º-1.4ºC; chl-a ~ 0.6-0.8 mg m^{-3}). These climatological transects (Figure 10b) confirm an
730   earlier suggestion based on Figure 9, where the northward spatio-temporal migration of the chl-a bloom is apparent. Here we note that the highest chl-a concentrations along the three climatological transects occur around December in T-I, through December to February in T-II and around February in T-III.

In summary, the remotely-sensed observations of SST and chl-a concentrations have proven to be of great potential to
735   monitor major features of the chl-a blooms in the BS accounting for a biophysical coupling between two hydrographic scenarios (TBW and TWW pools) confronted along the PF. Importantly, we recall these two hydrographic scenarios embed different phytoplankton assemblages, as it has been discussed based on previous literature and results from this study.
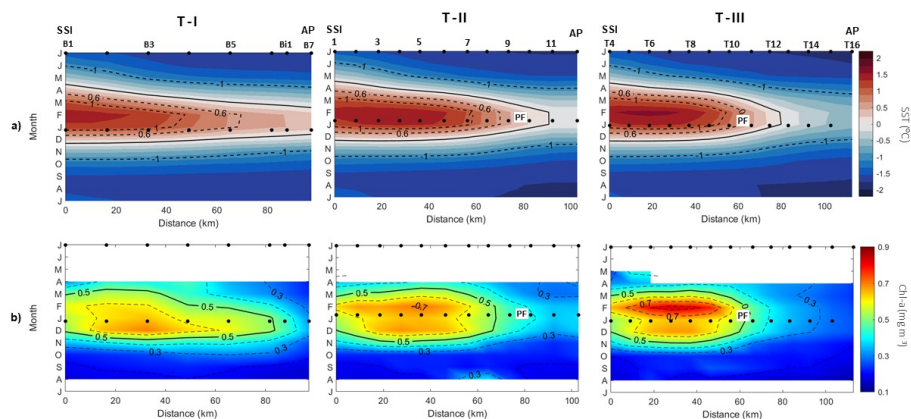
Figure 10. Monthly climatology from 1998 to 2018 of a) Sea Surface Temperature (SST), and b) chlorophyll-a (chl-a) concentration for each study transect
740   (see Figures 2-4) from the South Shetland Islands (SSI) to the Antarctic Peninsula (AP). The black markers (dots) situated at the top of the subplots represent the station's positions along the transects. These same stations are also displayed during the summer months when the cruises were carried out. Additionally, the position of the Peninsula Front(PF), as identified during the cruises and located along the isopycnal of 27.55 kg m^{-3}, is also indicated.

Lastly, it is worthwhile noting that the alignment of the chl-a spatial distribution along an oceanic front is not a novel feature
745   in the world's oceans, and has been already investigated in the literature (Moore and Abbott, 2002; Baird *et al*., 2008; Von

Bodungen *et al*., 2008). Thus, the novelty of our work lies in demonstrating through *in situ* observations and remotely-sensed measurements that such a biophysical coupling has the potential to be used to monitor the chl-a blooms and phytoplankton assemblages occurring seasonally in BS. This aspect is particularly relevant because BS is a key region for the sustainability of Antarctic marine ecosystem, which is challenging to monitor due to the hazardous prevailing conditions in polar regions.

750 In future studies, we expect the calculation of the frontal probability (Yang *et al.*, 2023) of the PF through a multi-year time-series of SST data may be beneficial to assess and co-locate interannually the alignment of the thermal front and the chl-a bloom domains using an automated algorithm for the Bransfield Strait study case (see Appendix B for further insights).

4 Conclusions

755 In this study, we address the hypothesis that the spring-to-summertime biophysical coupling controlling the chl-a bloom in the BS could be monitored through a combination of remotely-sensed observations of chl-a and SST, which strongly conditions the spatio-temporal variability of the phytoplankton assemblage across the PF. Our approach is based on the characterisation of climatological fields, following the motivation from novel and historical synoptic *in situ* observations which reveal that the PF may be used as a guideline to contour two distinctive niches for phytoplankton assemblage in the

760 BS, both horizontally and vertically.

Based on remotely-sensed climatologies, we find that the surface distribution of the seasonal variation of the SST and chl-a in the BS enables the identification of two environmentally different scenarios for the phytoplankton, which then grow under different strategies following the revised literature.

765 The first scenario is the pool of Transitional Bellingshausen Water, relatively warmer and less saline waters in a stratified water column with shallow mixed layers as compared to the second scenario. The second scenario is the pool of Transitional Weddell Water, relatively colder and more saline waters in a well-mixed water column with deeper mixed layers. We identify that the climatological isotherm characterising the PF location at surface during the summer months corresponds to 0.6ºC isotherm, which divides the BS in two domains. This division is further supported when we show that the isoline of 0.5

770 mg m^{-3} concentration of chl-a aligns with the 0.6ºC isotherm, which works well as a threshold contouring the chl-a bloom around the SSI and embedding coherently in space the region with highest chl-a values during the summer months.

Following the seasonal climatology of the SIC, we notice that the larger freshwater inputs reported in the literature over the TBW domain and contributing to the vertical stabilization of the water column might be driven by a warmer oceanic forcing

775 over coastal/glacial areas of the SSI (Cook *et al.*, 2016; Saenz *et al.*, 2023) rather than by melting of the open ocean sea-ice.

On the other hand, the seasonal climatology of the wind stress forcing suggests that the westerlies may play a major role in contributing to (1) stratified waters on the TBW domain via downwelling-favourable Ekman transport along the southern SSI shelf, through which the Bransfield Current flows; and (2) well-mixed upper layers on the TWW domain via upwelling-favourable Ekman transport along the west AP shelf.

Moreover, based on *ad hoc* study boxes located according to the spatial distribution of the remotely-sensed chl-a concentrations, we conclude that two different climatological chl-a blooms developing simultaneously but of different *nature* (i. e. phytoplankton assemblage) can be identified in the BS, as suggested by their different intensity and timing (month of initiation and rate of increase). This is in agreement with former results in a series of studies which reported that cryptophytes compete in the BS primarily with diatoms and other nanophytoplanton groups (Mura *et al.*, 1995; García *et al.*, 2013; Mendes *et al.*, 2013; Gonçalves-Araujo *et al.*, 2015; Mukhanov *et al.*, 2021; Costa *et al.*, 2023; Mendes *et al.*, 2023), following strategies to adapt better to the physical environment present through that year, and which display differently by zones in the monthly climatologies of SST, air temperature, SIC and wind stress forcing. Generally speaking, these studies have reported that TBW chl-a concentrations are commonly characterised by cryptophytes and small diatoms, while TWW chl-a concentrations are more frequently characterised by large diatoms.

We also note that the biophysical coupling between the chl-a blooms at both sides of the PF is largely the result of interannually varying physical properties determined by the TBW and TWW pools, as we revisit our results against the existing literature on phytoplankton assemblage in the BS. This suggests that the combined analysis of remotely-sensed observations of chl-a and SST (as presented in this study) may be of help in elucidating the spatio-temporal variability of the two blooms occurring in the BS during the summer months from year to year. Nevertheless, we must note that a given uncertainty will still exist about knowing which phytoplankton community may be dominating from year to year the TBW and the TWW pools, unless existing remotely-sensed phytoplankton assemblage products are further validated in the future. We have explored such products (not shown), but the lack of a product detecting only cryptophytes hampers the assessment of their year-to-year competition with diatoms (a product which actually exists) in the BS. We find this is of paramount importance for a more comprehensive understanding of the marine ecosystem composition in the BS.

Lastly, we conclude that combined analyses of remotely-sensed observations of SST and chl-a concentrations have a great potential to capture major features of the chl-a blooms in the BS accounting for a biophysical coupling between two hydrographic scenarios (TBW and TWW pools) confronted along and across the PF. We think that these results highlight the importance of long-term monitoring of the spatio-temporal distribution of the chl-a blooms in the BS using satellite measurements of SST and chl-a. Such monitoring may prove pivotal for future studies investigating the forcings driving the long-term variability of the phytoplankton assemblage in the BS.

Deleted: Through Section 3.3, and

Deleted: In Section 3.4, we revised our results against the literature about phytoplankton assemblage in the BS, and …

Deleted: conclude

Deleted: through Section 3.5

Acknowledgements

This work has been supported by the Spanish government (Ministerio de Economía y Competitividad) through the projects e-IMPACT (PID2019-109084RB-C21), CIEMAR (29HE19991212), and COUPLING (CTM2008-06343-CO2-01). The first author is also grateful to the Canary government (Consejería de Economía, Conocimiento y Empleo, Agencia Canaria de Investigación, Innovación y Sociedad de la Información) for the financial support awarded through a PhD scholarship (TESIS2021010025). We are grateful to the constructive and careful review and editorial work performed by Reviewer #1, the Editor Dr. Xinping Hu and Executive Editor Dr. Bernadette Sloyan. ChatGPT, developed by OpenAI, was used for proofreading of this manuscript.

References

Aracena, C., González, H. E., Garcés-Vargas, J., Lange, C. B., Pantoja, S., Muñoz, F., Teca E., and Tejos, E.: Influence of summer conditions on surface water properties and phytoplankton productivity in embayments of the South Shetland Islands, Polar Biol., 41, 2135-2155, https://doi.org/10.1007/s00300-018-2338-x, 2018.

Arrigo, K. R., Worthen, D., Schnell, A., and Lizotte, M. P.: Primary production in Southern Ocean waters, J. Geophys. Res.-Oceans, 103, 15587-15600, https://doi.org/10.1029/98JC00930, 1998.

Baird, M. E., Timko, P. G., Middleton, J. H., Mullaney, T. J., Cox, D. R., and Suthers, I. M.: Biological properties across the Tasman Front off southeast Australia, Deep Sea Res. Part I Oceanogr. Res. Pap., 55, 1438-1455, 2008.

Basterretxea, G., and Arístegui, J.: Phytoplankton biomass and production during late austral spring (1991) and summer (1993) in the Bransfield Strait, Polar Biol., 21, 11-22, https://doi.org/10.1007/s003000050328, 1999.

Berdalet, E., Vaqué, D., Arin, L., Estrada, M., Alcaraz, M., and Fernández, J. A.: Hydrography and biochemical indicators of microplankton biomass in the Bransfield Strait (Antarctica) during January 1994, Polar Biol., 17, 31-38, https://doi.org/10.1007/s003000050102, 1997.

Brown, M. S., Munro, D. R., Feehan, C. J., Sweeney, C., Ducklow, H. W., and Schofield, O. M.: Enhanced oceanic CO_2 uptake along the rapidly changing West Antarctic Peninsula, Nat. Clim. Change, 9, 678-683, https://doi.org/10.1038/s41558-019-0552-3, 2019.

Canny, J.: A computational approach to edge detection, IEEE Trans. Pattern Anal. Mach. Intell., (6), 679-698, https://doi.org/10.1109/TPAMI.1986.4767851, 1986.

Catalán, I. A., Morales-Nin, B., Rotllant, G., Palomera, I., and Emelianov, M.: Environmental influences on zooplankton and micronekton distribution in the Bransfield Strait and adjacent waters, Polar Biol., 31, 691-707, https://doi.org/10.1007/s00300-008-0408-1, 2008.

Chisholm, S. W., and Morel, F. M.: What controls phytoplankton production in nutrient-rich areas of the open sea?, Limnol. Oceanogr., 36, 1507–1511, 1991.

Comiso, J. C., Maynard, N. G., Smith Jr, W. O., and Sullivan, C. W.: Satellite ocean color studies of Antarctic ice edges in summer and autumn, J. Geophys. Res.- Oceans, 95, 9481-9496, https://doi.org/10.1029/JC095iC06p09481, 1990.

Corzo, A., Rodríguez-Gálvez, S., Lubian, L., Sobrino, C., Sangrà, P., and Martínez, A.: Antarctic marine bacterioplankton subpopulations discriminated by their apparent content of nucleic acids differ in their response to ecological factors, Polar Biol., 29, 27-39, https://doi.org/10.1007/s00300-005-0032-2, 2005.

Costa, R. R., Ferreira, A., de Souza, M. S., Tavano, V. M., Kerr, R., Secchi, E. R., Brotas, V., Dotto, T. S., Brito, A. C., and Mendes, C. R. B.: Physical-biological drivers modulating phytoplankton seasonal succession along the Northern Antarctic Peninsula, Environ. Res., 231, 116273, https://doi.org/10.1016/j.envres.2023.116273, 2023.

Dotto, T.S., Mata, M. M., Kerr, R., and Garcia, C. A.: A novel hydrographic gridded data set for the northern Antarctic Peninsula, Earth Syst. Sci. Data, 13, 671-696, https://doi.org/10.5194/essd-13-671-2021, 2021.

Ducklow, H. W., Erickson, M., Kelly, J., Montes-Hugo, M., Ribic, C. A., Smith, R. C., Stammerjohn, S. E., and Karl, D. M.: Particle export from the upper ocean over the continental shelf of the west Antarctic Peninsula: A long-term record, 1992– 2007, Deep Sea Res. Part II Top. Stud. Oceanogr., 55, 2118-2131, https://doi.org/10.1016/j.dsr2.2008.04.028, 2008.

Ducklow, H. W., Fraser, W. R., Meredith, M. P., Stammerjohn, S. E., Doney, S. C., Martinson, D. G., Sailley, S. F., Schofield, O. M., Steinberg, D. K., Venables, H. J., and Amsler, C. D.: West Antarctic Peninsula: an ice-dependent coastal marine ecosystem in transition, Oceanography, 26, 190-203, https://doi.org/10.5670/oceanog.2013.62, 2013.

Eayrs, C., Holland, D., Francis, D., Wagner, T., Kumar, R., and Li, X.: Understanding the Seasonal Cycle of Antarctic Sea Ice Extent in the Context of Longer-Term Variability, Rev. Geophys., 57, 1037-1064, https://doi.org/10.1029/2018RG000631, 2019.

El-Sayed, S. Z.: On the productivity of the southwest Atlantic Ocean and the waters west of the Antarctic Peninsula, Biology of the Antarctic Seas III Antar. Res. Ser., 11, 15-47, https://doi.org/10.1029/AR011p0015, 1967.

El-Sayed, S. Z.: History and evolution of primary productivity studies of the Southern Ocean, Polar Biol., 28, 423-438, https://doi.org/10.1007/s00300-004-0685-2, 2005.

García, M. A., López, O., Sospedra, J., Espino, M., Gracia, V., Morrison, G., Rojas, P., Figa, J., Puigdefabregas, J., and Arcilla, A. S.: Mesoscale variability in the Bransfield Strait region (Antarctica) during Austral summer, Ann. Geophys., 12, 856-867, https://doi.org/10.1007/s00585-994-0856-z, 1994.

García, M. A., Castro, C. G., Ríos, A. F., Doval, M. D., Rosón, G., Gomis, D., and López, O.: Water masses and distribution of physico-chemical properties in the Western Bransfield Strait and Gerlache Strait during Austral summer 1995/96, Deep Sea Res. Part II Top. Stud. Oceanogr., 49, 585-602, https://doi.org/10.1016/S0967-0645(01)00113-8, 2002.

García-Muñoz, C., Lubián, L. M., García, C. M., Marrero-Díaz, Á., Sangra, P., and Vernet, M.: A mesoscale study of phytoplankton assemblages around the South Shetland Islands (Antarctica), Polar Biol., 36, 1107-1123, https://doi.org/10.1007/s00300-013-1333-5, 2013.

Garibotti, I. A., Vernet, M., Ferrario, M. E., Smith, R. C., Ross, R. M., and Quetin, L. B.: Phytoplankton spatial distribution patterns along the western Antarctic Peninsula (Southern Ocean), Mar. Ecol. Prog. Ser., 261, 21-39, https://doi.org/10.3354/meps261021, 2003.

Gill, A. E.: Atmosphere-Ocean Dynamics, Academic Press, 30, 662, 1982.

Grelowski, A., Majewicz, A., and Pastuszak, M.: Mesoscale hydrodynamic processes in the region of Bransfield Strait and the southern part of Drake Passage during BIOMASS-SIBEX 1983/84, Polish Polar Res., 353-369, 1986.

Gonçalves-Araujo, R., de Souza, M. S., Tavano, V. M., and Garcia, C. A. E.: Influence of oceanographic features on spatial and interannual variability of phytoplankton in the Bransfield Strait, Antarctica, J. Mar. Syst., 142, 1-15, https://doi.org/10.1016/j.jmarsys.2014.09.007, 2015.

Good, S., Fiedler, E., Mao, C., Martin, M. J., Maycock, A., Reid, R., Roberts-Jones, J., Searle, T., Waters, J., While, J., and Worsfold, M.: The current configuration of the OSTIA system for operational production of foundation sea surface temperature and ice concentration analyses, Remote Sens., 12, 720, https://doi.org/10.3390/rs12040720, 2020.

Haberman, K. L., Ross, R. M., and Quetin, L. B.: Diet of the Antarctic krill (Euphausia superba Dana): II. Selective grazing in mixed phytoplankton assemblages, J. Exp. Mar. Biol. Ecol., 283, 97-113, https://doi.org/10.1016/S0022-0981(02)00467-7, 2003.

Hernández-León, S., Sangrà, P., Lehette, P., Lubián, L., Almeida, C., Putzeys, S., Bécognée, P., and Andrade, M. P.: Zooplankton biomass and metabolism in the frontal zones of the Bransfield Strait, Antarctica, , J. Mar. Syst., 111, 196-207, https://doi.org/10.1016/j.jmarsys.2012.11.001, 2013.

Hersbach, H., Bell, B., Berrisford, P., Hirahara, S., Horányi, A., Muñoz Sabater, J., Nicolas, J., Peubey, C., Radu, R., Schepers, D., Simmons, A., Soci, C., Abdalla, S., Abellan, X., Balsamo, G., Bechtold, P., Biavati, G., Bidlot, J., Bonavita, M., De Chiara, G., Dahlgren, P., Dee, D., Diamantakis, M., Dragani, R., Flemming, J., Forbes, R., Fuentes, M., Geer, A., Haimberger, L., Healy, S., Hogan, R. J., Holm, E., Janiskova, M., Keeley, S., Laloyaux, P., Lopez, P., Lupu, C., Radnoti, G., de Rosnay, P., Rozum, I., Vamborg, F., Villaume, S., and Thépaut, J. N.: The ERA5 global reanalysis, Q. J. Roy. Meteorol. Soc., 146, 1999–2049, https://doi.org/10.1002/qj.3803, 2020.

Hewes, C. D., Reiss, C. S., and Holm-Hansen, O.: A quantitative analysis of sources for summertime phytoplankton variability over 18 years in the South Shetland Islands (Antarctica) region, Deep Sea Res. Part I Oceanogr. Res. Pap., 56, 1230-1241, https://doi.org/10.1016/j.dsr.2009.01.010, 2009.

Hofmann, E. E., Klinck, J. M., Lascara, C. M., and Smith, D. A.: Water mass distribution and circulation west of the Antarctic Peninsula and including Bransfield Strait, Foundations for ecological research west of the Antarctic Peninsula, 70, 61-80, 1996.

Holland, P. R., and Kwok, R.: Wind-driven trends in Antarctic sea-ice drift, Nature Geosci., 5, 872-875, https://doi.org/10.1038/ngeo1627, 2012.

Holland, P. R.: The seasonality of Antarctic sea ice trends, Geophys. Res. Lett., 41, 4230-4237, https://doi.org/10.1002/2014GL060172, 2014.

Holte, J., and Talley, L.: A new algorithm for finding mixed layer depths with applications to Argo data and Subantarctic Mode Water formation, J.. Atmos. Ocean. Technol., 26, 1920-1939, https://doi.org/10.1175/2009JTECHO543.1, 2009.

Kara, A. B., Wallcraft, A. J., Metzger, E. J., Hurlburt, H. E., and Fairall, C. W.: Wind stress drag coefficient over the global
955 ocean, J. Clim., 20, 5856-5864, https://doi.org/10.1175/2007JCLI1825.1, 2007.

Kusahara, K., Williams, G. D., Massom, R., Reid, P., and Hasumi, H.: Spatiotemporal dependence of Antarctic sea ice variability to dynamic and thermodynamic forcing: A coupled ocean–sea ice model study, Clim. Dyn., 52, 3791-3807, https://doi.org/10.1007/s00382-018-4348-3, 2019.
960

La, H., Park, K., Chae, J. Y., Park, T., and Park, J.: Climatic factors and their robust evidences controlling phytoplankton biomass in the Bransfield Strait, Terr. Atmos. Ocean. Sci., 30, 821-830, http://doi.org/10.3319/TAO.2019.04.30.01, 2019.

Large, W. G., and Pond, S.: Open ocean momentum flux measurements in moderate to strong winds, J. Phys. Oceanogr., 11,
965 324-336, https://doi.org/10.1175/1520-0485(1981)011%3C0324:OOMFMI%3E2.0.CO;2, 1981.

Lee, E. Y., and Park, K. A.: Validation Satellite Sea Surface Temperature in the Coastal Regions, IEEE International Geoscience and Remote Sensing Symposium IGARSS, Brussels, Belgium, 11-16 July 2021, 7607-7610, http://doi.org/10.1109/IGARSS47720.2021.9553695, 2021.
970

Lipski, M., and Rakusa-Suszczewski, S.: Early summer pattern of vertical distribution of chlorophyll-a (Bransfield Strait, Antarctica, November 1986), Pol. Arch. Hydrobiol., 37, 287-293, 1990.

Loeb, V., Siegel, V., Holm-Hansen, O., Hewitt, R., Fraser, W., Trivelpiece, W., and Trivelpiece, S.: Effects of sea-ice
975 extentg and krill or salp dominance on the Antarctic food web, Nature, 387, 897-900, https://doi.org/10.1038/43174, 1997.

López, O., García, M. A., Gomis, D., Rojas, P., Sospedra, J., and Sánchez-Arcilla, A., Hydrographic and hydrodynamic characteristics of the eastern basin of the Bransfield Strait (Antarctica), Deep Sea Res. Part I Oceanogr. Res. Pap., 46, 1755-1778, https://doi.org/10.1016/S0967-0637(99)00017-5, 1999.
980

Macías, D., Rodríguez-Santana, Á., Ramírez-Romero, E., Bruno, M., Pelegrí, J. L., Sangrà, P., Aguiar-González, B., and García, C. M.: Turbulence as a driver for vertical plankton distribution in the subsurface upper ocean, Sci. Mar, 77, 541-549, https://doi.org/10.3989/scimar.03854.03A, 2013.

985 Mackey, M. D., Mackey, D. J., Higgins, H. W., and Wright, S. W.: CHEMTAX-a program for estimating class abundances from chemical markers: application to HPLC measurements of phytoplankton, Mar. Ecol. Prog. Ser., 144, 265-283, https://doi.org/10.3354/meps144265, 1996.

Marrari, M., Hu, C., and Daly, K.: Validation of SeaWiFS chlorophyll-a concentrations in the Southern Ocean: A
990 revisit, Remote Sens. Environ., 105, 367-375, https://doi.org/10.1016/j.rse.2006.07.008, 2006.

Mendes, C. R. B., Tavano, V. M., Leal, M. C., de Souza, M. S., Brotas, V., and Garcia, C. A. E.: Shifts in the dominance between diatoms and cryptophytes during three late summers in the Bransfield Strait (Antarctic Peninsula), Polar Biol., 36, 537-547, https://doi.org/10.1007/s00300-012-1282-4, 2013.
995
Mendes, C. R. B., Costa, R. R., Ferreira, A., Jesus, B., Tavano, V. M., Dotto, T. S., Leal, M.C., Kerr, R., Islabão, C.A., Franco, A.D., Mata, M. M., and Secchi, E. R.: Cryptophytes: An emerging algal group in the rapidly changing Antarctic Peninsula marine environments, Global Change Biol., 29, 1791-1808, https://doi.org/10.1111/gcb.16602, 2023.

1000 Mitchell, B. G., and Holm-Hansen, O.: Observations of modeling of the Antartic phytoplankton crop in relation to mixing depth, Deep Sea Res. Part I. Oceanogr. Res. Pap., 38, 981-1007, https://doi.org/10.1016/0198-0149(91)90093-U, 1991.

Montes-Hugo, M., Doney, S. C., Ducklow, H. W., Fraser, W., Martinson, D., Stammerjohn, S. E., and Schofield, O.: Recent changes in phytoplankton communities associated with rapid regional climate change along the western Antarctic
1005 Peninsula, Science, 323, 1470-1473, https://doi.org/10.1126/science.1164533, 2009.

Moore, J. K., and Abbott, M. R.: Surface chlorophyll concentrations in relation to the Antarctic Polar Front: seasonal and spatial patterns from satellite observations, J. Mar. Syst., 37, 69-86, 2002.

1010 Mukhanov, V. S., Sakhon, E. G., Polukhin, A. A., and Artemiev, V. A.: Nanophytoplankton in the Bransfield Strait: Contribution of Cryptophyta to the Community Abundance and Biomass During Austral Summer, in: Antarctic Peninsula Region of the Southern Ocean. Advances in Polar Ecology, edited by: Morozov, E.G., Flint, M.V., and Spiridonov, V.A., Springer, 261-276, https://doi.org/10.1007/978-3-030-78927-5_20, 2021.

1015 Mura, M. P., Satta, M. P., and Agustí, S.: Water-mass influences on summer Antarctic phytoplankton biomass and community structure, Polar Biol., 15, 15-20, https://doi.org/10.1007/BF00236119, 1995.

Niller, P. P., Amos, A., and Hu, J. H.: Water masses and 200 m relative geostrophic circulation in the western Bransfield Strait region, Deep Sea Res. Part I. Oceanogr. Res. Pap., 38, 943-959, https://doi.org/10.1016/0198-0149(91)90091-S, 1991.

1020

Petrou, K., Kranz, S. A., Trimborn, S., Hassler, C. S., Ameijeiras, S. B., Sackett, O., Ralph, P. J., and Davidson, A. T.: Southern Ocean phytoplankton physiology in a changing climate, J. Plant Physiol., 203, 135-150, https://doi.org/10.1016/j.jplph.2016.05.004, 2016.

1025 Polukhin, A. A., Morozov, E. G., Tishchenko, P. P., Frey, D. I., Artemiev, V. A., Borisenko, G. V., Vidnichuk, A. V., Marina, E. N., Medvedev, E. V., Popov, O. S., Seliverstova, A. M., and Chultsova, A. L.: Water Structure in the Bransfield Strait (Antarctica) in January 2020: Hydrophysical, Optical, and Hydrochemical Features, Oceanology, 61, 632-644, https://doi.org/10.1134/S0001437021050106, 2021.

1030 Prézelin, B. B., Hofmann, E. E., Mengelt, C., and Klinck, J. M.: The linkage between Upper Circumpolar Deep Water (UCDW) and phytoplankton assemblages on the west Antarctic Peninsula continental shelf, J. Mar. Res., 58, 165-202, https://doi.org/10.1357/002224000321511133, 2000.

Primo, C., and Vázquez, E.: Ascidians collected during the Spanish Antarctic expedition CIEMAR 99/00 in the Bransfield 1035 and Gerlache Straits, J. Nat. Hist., 41, 1775-1810, https://doi.org/10.1080/00222930701500126, 2007.

Patel, R. S.: Wind Stresses computation, MATLAB Central File Exchange, https://www.mathworks.com/matlabcentral/fileexchange/53391-wind-stresses-computation, 2023.

1040 Saenz, B. T., McKee, D. C., Doney, S. C., Martinson, D. G., and Stammerjohn, S. E.: Influence of seasonally varying sea-ice concentration and subsurface ocean heat on sea-ice thickness and sea-ice seasonality for a 'warm-shelf' region in Antarctica, J. Glaciol., 1-17, https://doi.org/10.1017/jog.2023.36, 2023.

Sailley, S. F., Ducklow, H. W., Moeller, H. V., Fraser, W. R., Schofield, O. M., Steinberg, D. K., Garzio, L. M., and Doney, 1045 S. C.: Carbon fluxes and pelagic ecosystem dynamics near two western Antarctic Peninsula Adélie penguin colonies: an inverse model approach, Mar. Ecol. Prog. Ser., 492, 253-272, https://doi.org/10.3354/meps10534, 2013.

Sangrà, P., Gordo, C., Hernández-Arencibia, M., Marrero-Díaz, A., Rodríguez-Santana, A., Stegner, A., Martínez-Marrero, A., Pelegrí, J., and Pichon, T.: The Bransfield current system, Deep Sea Res. Part I Oceanogr. Res. Pap., 58, 390-402, 1050 https://doi.org/10.1016/j.dsr.2011.01.011, 2011.

Sangrà, P., García-Muñoz, C., García, C. M., Marrero-Díaz, Á., Sobrino, C., Mouriño-Carballido, B., Aguiar-González, B., Henríquez-Pastene, C., Rodríguez-Santana, Á., Lubián, L. M., Hernández-Arencibia, M., Hernández-León, S., and Estrada-Allis, S. N.: Coupling between upper ocean layer variability and size-fractionated phytoplankton in a non-nutrient-limited environment, Mar. Ecol. Prog. Ser., 499, 35-46, https://doi.org/10.3354/meps10668, 2014.

Sangrà, P., Stegner, A., Hernández-Arencibia, M., Marrero-Díaz, Á., Salinas, C., Aguiar-González, B., Henríquez-Pastene C., and Mouriño-Carballido, B.: The Bransfield gravity current, Deep Sea Res. Part I Oceanogr. Res. Pap., 119, 1-15, https://doi.org/10.1016/j.dsr.2016.11.003, 2017.

Schofield, O., Ducklow, H. W., Martinson, D. G., Meredith, M. P., Moline, M. A., and Fraser, W. R.: How do polar marine ecosystems respond to rapid climate change?, Science, 328, 1520-1523, https://doi.org/10.1126/science.1185779, 2010.

Siegel, D. A., Doney, S. C., and Yoder, J. A.: The North Atlantic spring phytoplankton bloom and Sverdrup's critical depth hypothesis, Science, 296, 730-733, https://doi.org/10.1126/science.1069174, 2002.

Smith, R. C., Martinson, D. G., Stammerjohn, S. E., Iannuzzi, R. A., and Ireson, K.: Bellingshausen and western Antarctic Peninsula region: Pigment biomass and sea-ice spatial/temporal distributions and interannual variability, Deep Sea Res. Part II Top. Stud. Oceanogr., 55, 1949-1963, https://doi.org/10.1016/j.dsr2.2008.04.027, 2008.

Stammerjohn, S., Massom, R., Rind, D., and Martinson, D.: Regions of rapid sea ice change: An inter-hemispheric seasonal comparison, Geophys. Res. Lett., 39, https://doi.org/10.1029/2012GL050874, 2012.

Stenseth, N. C., Ottersen, G., Hurrell, J. W., Mysterud, A., Lima, M., Chan, K. S., Yoccoz, N. G., and Ådlandsvik, B.: Studying climate effects on ecology through the use of climate indices: the North Atlantic Oscillation, El Nino Southern Oscillation and beyond, Proc. R. Soc. B: Biol. Sci., 270, 2087-2096, https://doi.org/10.1098/rspb.2003.2415, 2003.

Sullivan, C. W., Arrigo, K. R., McClain, C. R., Comiso, J. C., and Firestone, J.: Distributions of phytoplankton blooms in the Southern Ocean, Science, 262, 1832-1837, https://doi.org/10.1126/science.262.5141.1832, 1993.

Thomalla, S. J., Fauchereau, N., Swart, S., and Monteiro, P. M. S.: Regional scale characteristics of the seasonal cycle of chlorophyll in the Southern Ocean, Biogeosciences, 8, 2849-2866, https://doi.org/10.5194/bg-8-2849-2011, 2011.

Tokarczyk, R.: Classification of water masses in the Bransfield Strait and southern part of the Drake Passage using a method of statistical multidimensional analysis, Polish Polar Res., 333-366, 1987.

Trenberth, K. E., Large, W. G., and Olson, J. G.: The mean annual cycle in global ocean wind stress, J. Phys. Oceanogr., 20, 1742–1760, https://doi.org/10.1175/1520-0485(1990)020%3C1742:TMACIG%3E2.0.CO;2, 1990.

Veny, M., Aguiar-González, B., Marrero-Díaz, Á., and Rodríguez-Santana, Á.: Seasonal circulation and volume transport of the Bransfield Current, Progress in Oceanography, 204, 102795, https://doi.org/10.1016/j.pocean.2022.102795, 2022.

Von Bodungen, B., John, H. C., Lutjeharms, J. R. E., Mohrholz, V., and Veitch, J.: Hydrographic and biological patterns across the Angola–Benguela Frontal Zone under undisturbed conditions, J. Mar. Syst., 74, 189-215, 2008.

Vorrath, M. E., Müller, J., Rebolledo, L., Cárdenas, P., Shi, X., Esper, O., Opel, T., Geibert, W., Muñoz, P., Haas, C., Kuhn, G., Lange, C. B., Lohmann, G., and Mollenhauer, G.: Sea ice dynamics in the Bransfield Strait, Antarctic Peninsula, during the past 240 years: a multi-proxy intercomparison study, Clim. Past, 16, 2459-2483, https://doi.org/10.5194/cp-16-2459-2020, 2020.

Xie, J., Zhu, J., and Li, Y.: Assessment and inter-comparison of five high-resolution sea surface temperature products in the shelf and coastal seas around China, Cont. Shelf Res., 28, 1286-1293, https://doi.org/10.1016/j.csr.2008.02.020, 2008.

Yang, K., Meyer, A., Strutton, P. G., & Fischer, A. M.: Global trends of fronts and chlorophyll in a warming ocean. *Commun. Earth & Environ.*, *4*(1), 489, https://doi.org/10.1038/s43247-023-01160-2, 2023.

Zhang, H. M., Reynolds, R. W., and Smith, T. M.: Bias characteristics in the AVHRR sea surface temperature, Geophys. Res. Lett., 31, https://doi.org/10.1029/2003GL018804, 2004.

Zhang, Y., Seidel, D. J., Golaz, J. C., Deser, C., and Tomas, R. A.: Climatological characteristics of Arctic and Antarctic surface-based inversions, J. Clim., 24, 5167-5186, https://doi.org/10.1175/2011JCLI4004.1, 2011.

Zhou, M., Niller, P. P., and Hu, J. H.: Surface currents in the Bransfield and Gerlache straits, Antarctica, Deep Sea Res. Part I Oceanogr. Res. Pap., 49, 267-280, https://doi.org/10.1016/S0967-0637(01)00062-0, 2002.

Zhou, M., Niller, P. P., Zhu, Y., and Dorland, R. D.: The western boundary current in the Bransfield Strait, Antarctica, Deep Sea Res. Part I Oceanogr. Res. Pap., 53, 1244-1252, https://doi.org/10.1016/j.dsr.2006.04.003, 2006.

Appendix A: Assessment of the SST products

1120   We assess the goodness of three available SST products by comparison with near-surface (0-1 m and 10 m depth) *in situ* temperature measurements collected from a variety of Antarctic cruises (Table A1). By linear regression, the coefficient of determination (R-squared) is used to evaluate the performance of the three satellite products, which are: (1) Optimally Interpolated SST (OI SST; https://www.remss.com/); (2) European Space Agency Climate Change Initiative (ESACCI; https://marine.copernicus.eu/); and, (3) Operational Sea Surface Temperature and Ice Analysis (OSTIA;

1125   https://marine.copernicus.eu/). For brevity, hereafter, we refer to the, as OI SST, ESACCI and OSTIA, respectively.

The grid spacing for OI SST is ~0.1º, but for both ESACCI and OSTIA is 0.05º. Meanwhile, temporal extent is also different, OI SST time range is from 01 June 2002 to present, ESACCI time range is from 01 September 1981 to 31 December 2016, and OSTIA time range is from 01 October 1981 to 31 May 2022.

1130

For a fair comparison, because the OI SST product starts globally in 2002, we first compare the three products to cruises GOAL (GOAL03, GOAL04 and GOAL05) and BREDDIES (2003), at two different depths (0-1 m and 10 m; see Table A2 to learn about the amount of profiles by depth level used in the analysis, and Table A3 to learn about the results). Based on the low coefficients found for OI SST as compared to ESACCI and OSTIA (Table A3), we decide to discard OI SST for

1135   further analysis.

Lastly, we use the entire dataset of available hydrographic observations (Table A1) in the study region, making a distinction between whether we use only data falling within Bransfield Strait (BS), Gerlache Strait (GS) or within both (full domain). These data are summarized in Table A4, where there are indications to the depth levels involved in the analysis: 0-1 m (8

1140   cruises with 539 stations from 1990 to 2010) and 10 m (21 cruises with 1,133 stations from 1990 to 2011).

Results in Table A5 show the lowest coefficients are found in Gerlache Strait for both ESACCI and OSTIA, while these values increase when including measurements from Bransfield Strait. To some extent, this agrees with the expectation provided the narrow nature of Gerlache Strait (~10 km at its narrowest part and ~50 km at its widest part). This implies the

1145   ocean in Gerlache Strait is in close proximity to land nearly everywhere, leading the discrepancies between remotely-sensed and *in situ* observations (Zhang *et al*., 2004; Xie *et al*., 2008; Lee and Park, 2021).

Notably, *in situ* measurements at 10 m present a higher correlation with satellite SST everywhere (Table A5). Given the similarity of correlation coefficients for ESACCI and OSTIA, we select OSTIA given its longer time record, which is from

1150   1981 to 2020 as opposed to ESACCI, which ends earlier in 2016 at the moment this analysis was performed in 2022.

CRUISE	DATES			
	Year	Month	Day	Season
M11_4 (*)	1990	Jan	01-10, 16	Summer
ANT-XII (PS33)	1994	Nov	26-30	Spring
		Dec	01-05	
FRUELA (*)	1995	Dec	03-23, 26-31	Spring
	1996	Jan	02-05, 18-31	Summer
		Feb	01-05	
ALMIRANTE IRIZAR	1996	May	08-09, 12-14	Autumn
ANT-XIV (PS42)	1996	Nov	15-28, 30	Spring
		Dec	01, 03-06, 08-24	
DOVETAIL	1997	Aug	04-23, 25-31	Winter
		Sep	01-05	
ANT-XV (PS49)	1998	Mar	31	Summer
		Apr	01-06, 17-22	Autumn
ALBATROSS (*)	1999	Mar	23-26, 31	Summer
		Apr	01-02	Autumn
CIEMAR	1999	Dec	15, 18-30	Spring
BREDDIES	2002	Dec	30-31	Spring
	2003	Jan	02-06, 11-14, 17-18, 21	Summer
GOAL03 (*)	2003	Jan	23-27, 29, 31	Summer
		Feb	21-23	
GOAL04 (*)	2004	Jan	18-29	Summer
GOAL05 (*)	2005	Jan	19, 21, 24-26, 28-31	Summer
		Feb	01-05, 07	
ANT-XXII (PS67)	2005	Mar	12-13, 15-19, 24, 31	Summer
		Apr	01-02	Autumn
SOS1 (*)	2008	Feb	21-29	Summer
		Mar	01-04	
ANT-XXIV (PS71)	2008	Mar	25-31	Summer
		Apr	01-05	Autumn
JC-031	2009	Feb	13-14, 16-18, 20-21	Summer
SOS2	2009	Feb	17-28	Summer
		Mar	01	
COUPLING	2010	Jan	08-26	Summer
SOS3 (*)	2010	Feb	16-24	Summer
ANT-XXVI (PS77)	2011	Jan	05-17	Summer

Table A1. Overview of the cruises used to calculate the coefficient of determination (see Section 2) and the dates they were carried out. Only cruises marked with an asterisk (*) provide data at depths of 0-1 m.

Cruise	Depth (m)	Profiles
GOAL03-04-05	0-1	190
	10	205
BREDDIES	10	61

Table A2. Number of profiles available in each cruise and depth used to analyse the goodness of available open-access remotely-sensed products of sea surface temperature.

1200

Cruise	Depth (m)	OISST	ESACCI	OSTIA
GOAL03-04-05 (BS and GS)	0-1	0.360	0.704	0.707
	10	0.258	0.574	0.512
BREDDIES (BS)	10	0.299	0.785	0.773

Table A3. R-squared coefficients for each SST satellite product (OI SST, ESACCI, OSTIA) compared to *in situ* SST data from four cruises' data at 0-1 m

1205 and 10 m depths (see amount of profiles in Table A2). The analysis is performed for different study regions: at the entire study region (BS and GS) and the Bransfield Strait (BS) surroundings (excluding the GS region).

	Depth (m)	Profiles
BS and GS	0-1	539
	10	1133
Gerlache Strait	0-1	417
	10	905
Bransfield Strait	0-1	122
	10	228

1210

Table A4. Same as Table A2, but here extended to eight cruises for depths of 0-1 m and twenty-one cruises for depths of 10 m. Regarding to Gerlache Strait region, there are only five cruises available for depths of 0-1 m (ALBATROSS, FRUELA, GOAL04, GOAL05, M11_4) and ten cruises for depths of 10 m (ALBATROSS, FRUELA, GOAL03, GOAL04, GOAL05, M11_4, ALMIRANTE IRIZAR, ANT_XXVII_PS77, CIEMAR, JC-031).

1215

Study Region	Depth (m)	ESACCI	OSTIA
		ESACCI	OSTIA
BS and GS	0-1	0.715	0.719
	10	0.787	0.784
Gerlache Strait	0-1	0.431	0.487
	10	0.515	0.546
Bransfield Strait	0-1	0.815	0.787
	10	0.857	0.849

Table A5. R-squared coefficients for each SST satellite product (ESACCI, OSTIA) compared to *in situ* SST data from eight cruises' data at depths of 0-1 m and twenty-one cruises' data at depths of 10 m (see amount of profiles in Table A4). The analysis is performed for different study regions: at the entire study region (BS and GS), only the Gerlache Strait (GS), and the Bransfield Strait (BS) surroundings (excluding the GS region).

Appendix B: Frontal probability of the Peninsula Front
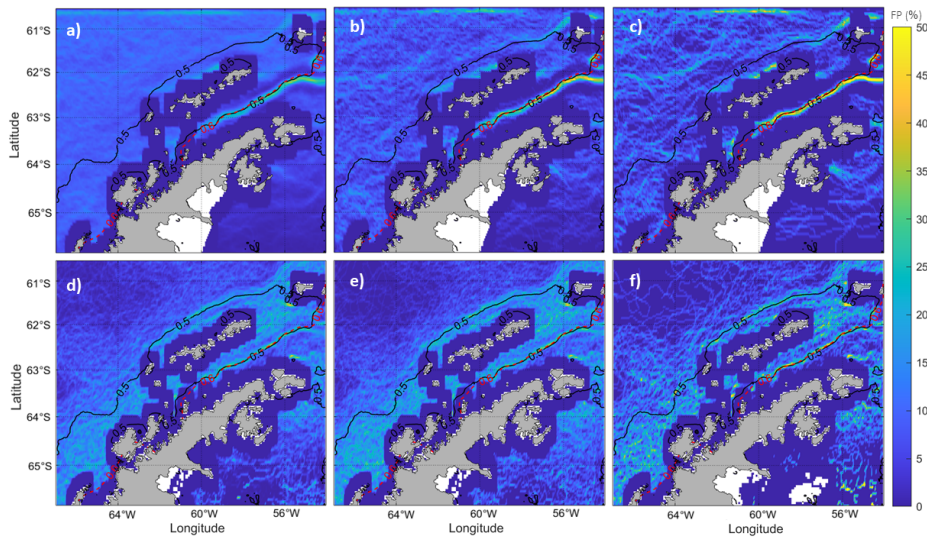
Figure B1. From left to right, the upper panels (a,b,c) show the Frontal Probability (FP) based on daily, monthly-averaged and seasonally-averaged data for sea surface temperature through 21 years of summertime. Lower panels (d,e,f) show the same as upper panels but based on chlorophyll-a (chl-a) concentrations. The climatological summertime isotherm of 0.6ºC (dashed red line) and the isoline of 0.5 mg m^{-3} chl-a concentrations (solid black line) as

obtained for Figures 5 and 7 highlight the goodness of our methodology to select them as characteristic environmental values contouring the Peninsula Front

1230 in Bransfield Strait.

Figure B1 presents the Frontal Probability (FP; Yang *et al.*, 2023) from the SST and chl-a fields in Bransfield Strait for the period 1998-2018. The Canny edge-detection algorithm (Canny, 1986) is applied to identify coherent frontal segments.

1235 Then, the summertime FP is calculated based on three different cases, using fronts detected on daily data, monthly-averaged data, and seasonally-averaged data over a period of 21 years (in all cases the information corresponds solely to summertime). The FP is defined at each pixel as a percentage where the times that the pixel is identified as a front is referred to the number of total valid pixels for a given time interval.

Results support the choice of the characteristic isotherms and isoline of chl-a used in this study to distinguish in the BS two

1240 different pools of chl-a development. Additionally, we note that the signal of the Peninsula Front increases in FP, especially in SST, when based on time-averaged fields (panels b,c,e,f) as compared to daily fields (a,d). We attribute this to the recurrence of the Peninsula Front, which gets better defined when a time-average procedure is followed before applying the Canny edge-detection algorithm. Simultaneously, a noisier signal emerges regarding other non-recurrent fronts which are present only occasionally in time-average fields, thus leading to their presence only in a few fields when computing the FP.

1245 We suggest that the FP may be used in future studies to code an automated algorithm capable of monitoring the chl-a blooms in Bransfield Strait based on remotely-sensed SST and chl-a data, using the South Shetland Islands and the Antarctic Peninsula as physical boundaries, and the Peninsula Front location as the oceanographic frontier contouring the TBW and TWW pools. Thus, co-locating interannually the alignment of the thermal front and the chl-a spatial distribution will enable the computation of accurate areas of integration for the assessment of the surface blooms acting in the Bransfield Strait.

1250